Author Manuscript

Author Manuscript

Author Manuscript

Author Manuscript

HHS Public Access

Author manuscript

Cell Rep. Author manuscript; available in PMC 2020 September 09.

Published in final edited form as:

Cell Rep. 2020 July 21; 32(3): 107893. doi:10.1016/j.celrep.2020.107893.

Cofilin Loss in *Drosophila* Muscles Contributes to Muscle Weakness through Defective Sarcomerogenesis during Muscle Growth

Mridula Balakrishnan[1,2], **Shannon F. Yu**[2], **Samantha M. Chin**[3], **David B. Soffar**[2], **Stefanie E. Windner**[2], **Bruce L. Goode**[3], **Mary K. Baylies**[1,2,4,*]

[1]Biochemistry & Structural Biology, Cell & Developmental Biology, and Molecular Biology (BCMB) Program, Weill Cornell Graduate School of Medical Sciences, New York, NY 10065, USA

[2]Developmental Biology Program, Sloan Kettering Institute, Memorial Sloan Kettering Cancer Center, New York, NY 10065, USA

[3]Department of Biology, Rosenstiel Basic Medical Science Research Center, Brandeis University, Waltham, MA 02454, USA

[4]Lead Contact

SUMMARY

Sarcomeres, the fundamental contractile units of muscles, are conserved structures composed of actin thin filaments and myosin thick filaments. How sarcomeres are formed and maintained is not well understood. Here, we show that knockdown of *Drosophila* cofilin (*DmCFL*), an actin depolymerizing factor, disrupts both sarcomere structure and muscle function. The loss of *DmCFL* also results in the formation of sarcomeric protein aggregates and impairs sarcomere addition during growth. The activation of the proteasome delays muscle deterioration in our model. Furthermore, we investigate how a point mutation in CFL2 that causes nemaline myopathy (NM) in humans affects CFL function and leads to the muscle phenotypes observed *in vivo*. Our data provide significant insights to the role of CFLs during sarcomere formation, as well as mechanistic implications for disease progression in NM patients.

In Brief

How sarcomeres are added and maintained in a growing muscle cell is unclear. Balakrishnan et al. observed that *Dm*CFL loss in growing muscles affects sarcomere size and addition through

This is an open access article under the CC BY-NC-ND license (http://creativecommons.org/licenses/by-nc-nd/4.0/).

[*]**Correspondence:** m-baylies@ski.mskcc.org.

AUTHOR CONTRIBUTIONS

M.B. and M.K.B. conceived and designed the study. M.B. performed all of the experiments. S.F.Y. identified the phenotype. S.M.C. performed all of the single-molecule studies and was supervised by B.L.G. D.B.S. helped with transformants and western blotting. S.E.W. analyzed the data. M.B. and M.K.B. wrote the paper, with input from all of the authors, especially S.E.W. M.K.B. acquired the funding and supervised the study.

SUPPLEMENTAL INFORMATION

Supplemental Information can be found online at https://doi.org/10.1016/j.celrep.2020.107893.

DECLARATION OF INTERESTS

The authors declare no competing interests.

Author Manuscript Author Manuscript Author Manuscript Author Manuscript

unregulated actin polymerization. This results in a collapse of sarcomere and muscle structure, formation of large protein aggregates, and muscle weakness.

Graphical abstract

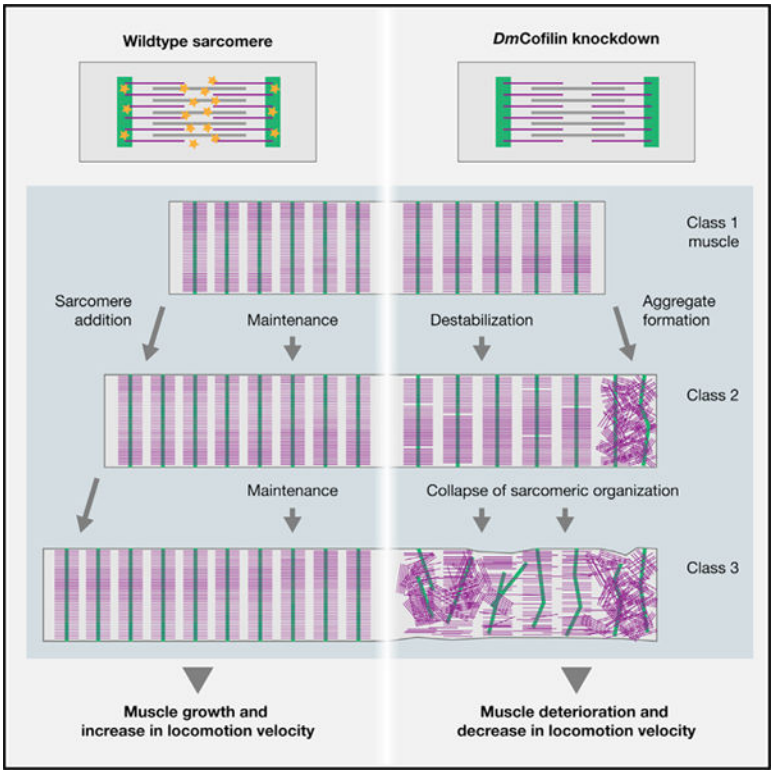

INTRODUCTION

Skeletal muscle cells, or myofibers, are highly organized cells that are necessary for locomotion. Each myofiber contains many linear myofibrils, which are composed of a repeated array of sarcomeres, the fundamental contractile units of the muscle cell. The coordinated contraction of all sarcomeres along the myofibril shortens the myofiber and produces mechanical force. Sarcomeres are conserved among metazoans and have been studied for decades (Ehler and Gautel, 2008). However, much remains unknown as to how sarcomeres are assembled and incorporated into myofibrils during muscle development and growth.

Sarcomeres consist of three structural elements: Z discs, thin filaments, and thick filaments (Figure 1A) (reviewed in Henderson et al., 2017). The Z discs define the lateral sarcomere boundaries and are composed of electron-dense proteins, including α-actinin and ZASP/Cypher (Masaki et al., 1967). The thin filaments are anchored at the Z discs and extend toward the middle of the sarcomere (M-line). Thin filaments comprise primarily actin and actin-binding proteins, such as nebulin and the troponin-tropomyosin complex (Katrukha, 2013; Labeit and Kolmerer, 1995). The actin filaments are capped at their pointed (minus) ends by tropomodulin (Tmod) and at their barbed (plus) ends by CapZ, which also anchors

Author Manuscript Author Manuscript Author Manuscript Author Manuscript

the thin filaments at the Z disc (Casella et al., 1986, 1987). The thick filaments are at the center of the sarcomere and are composed primarily of myosin and myosin-associated proteins (Bennett et al., 1986; Ruppel and Spudich, 1996; Sellers, 2000). Thick filaments interact with thin filaments and are crosslinked at the M-line, which is composed of proteins such as obscurin (Young et al., 2001). While many conserved sarcomeric proteins have been identified, their incorporation into and function within the sarcomere are not completely understood. Moreover, it is still unclear as to how sarcomere size is regulated and maintained. Understanding these fundamental aspects of muscle biology is crucial, as mutations in sarcomeric proteins have been implicated in several muscle diseases.

A skeletal muscle disease with links to sarcomere structure and sarcomeric proteins is nemaline myopathy (NM). NM has an incidence of 1 in 50,000 births and manifests as difficulties in breathing and swallowing, hypotonia, delayed motor development, and atrophied muscle fibers (Maggi et al., 2013; Malfatti and Romero, 2016; Sewry et al., 2019; Wallgren-Pettersson et al., 1999, 2004). Not all skeletal muscles are affected equally in NM patients (Malfatti and Romero, 2016). A characteristic feature of affected muscles is electron-dense protein aggregates within the muscle fibers, called nemaline (rod) bodies. These aggregates are composed of sarcomeric proteins, such as α-actinin and α-actin, and are thought to be extensions of the Z disc (Cassandrini et al., 2017; Jockusch et al., 1980; Romero et al., 2013; Sewry et al., 2019; Wallgren-Pettersson et al., 1995; Yamaguchi et al., 1982). While nemaline bodies are the key diagnostic feature of NM, there is no correlation between nemaline body number and disease severity (Malfatti and Romero, 2016). Mutations in at least 12 genes have been implicated in NM: 8 of the 12 genes encode sarcomere thin filament proteins, including ACTA1, NEB, TPM2, TPM3, CFL2, TPM3, LMOD3, TNNT1, and TNNT3; 3 genes encode Kelch-like proteins, namely KBTBD13, KLHL40, and KLHL41; and 1 gene encodes MYPN, a component of the Z disc (Gupta and Beggs, 2014; Kondo et al., 2012; Malfatti and Romero, 2016; Miyatake et al., 2017; Nilipour et al., 2018; Sandaradura et al., 2018; Sewry et al., 2019). It remains unclear how mutations in these individual genes contribute to NM development and particularly to the mechanisms that result in the formation of nemaline bodies and muscle weakness.

One gene mutated in NM patients is *CFL2*, which encodes a member of the actin-depolymerizing factor (ADF)/cofilin family of proteins (Agrawal et al., 2007; Ockeloen et al., 2012; Ong et al., 2014). Humans possess 3 ADF/cofilin family members: ADF/*DSTN* (*Destrin*), *CFL1* (*Cofilin-1*), and *CFL2* (*Cofilin-2*). *CFL2* is expressed in mature skeletal muscle, and its loss results in aberrant skeletal muscle structure and early lethality (Agrawal et al., 2012; Ockeloen et al., 2012). CFL2 binds to globular actin monomers (G-actin) to inhibit nucleotide exchange (ADP to ATP) and to filamentous actin (F-actin) to promote their fragmentation and disassembly into monomers (Vartiainen et al., 2002). *CFL2* directly severs actin filaments and is thought to regulate sarcomere thin filament length (Chin et al., 2016; Kremneva et al., 2014). While the structure and function of CFL2 have been identified, how mutations in CFL2 contribute to the pathogenesis of NM is not well understood.

A yeast two and half-hybrid screen in our lab identified *twinstar* (*tsr*) as a putative regulator of muscle formation. Tsr is a *Drosophila* homolog of the ADF/cofilin family of proteins and

Author Manuscript Author Manuscript Author Manuscript Author Manuscript

has the highest sequence homology to human cofilin-2 (*CFL2*; Edwards et al., 1994; Gunsalus et al., 1995). Tsr functions in cytokinesis, axonal growth, and in the planar cell polarity pathway (Blair et al., 2006; Gunsalus et al., 1995; Ng and Luo, 2004). Here, we report a new role for Tsr (referred to as *Dm*CFL) in regulating both larval sarcomere and myofiber structure. Our data suggest that *Dm*CFL is required to regulate actin filament length and the size of existing sarcomeres. *Dm*CFL is also required to regulate actin filament addition in newly formed sarcomeres during muscle growth. In accordance with the role of *Dm*CFL in both these processes, muscle-specific knockdown of *Dm*CFL results in a progressive loss of sarcomere and muscle fiber integrity. In addition, we observe protein aggregates within affected muscle fibers and directly link progressive muscle deterioration to deficits in locomotion behavior. Furthermore, we demonstrate that increasing proteasome activity improves muscle structure and function in *Dm*CFL-knockdown muscles. Finally, we show functional similarities between *Drosophila* and human cofilin proteins through *in vitro* and *in vivo* analyses and model a specific mutation found in a human NM patient. Our data provide significant insights to the role of CFL2 during muscle growth, as well as mechanistic implications for disease progression in NM patients.

RESULTS

Muscle-Specific Knockdown of *Dm*CFL Disrupts Muscle Structure and Function

The *Drosophila* larval musculature consists of a repeated pattern of hemisegments along the body wall, each of which consists of 30 unique muscles of different shapes, sizes, and orientations (Figure 1B). Each larval muscle is a single cell or fiber, enabling easy visualization of the muscle fiber structure (Bate, 1990). The larva progresses through 3 developmental stages, known as instars (5 days at 25°C), during which the muscles grow 25- to 40-fold (Demontis and Perrimon, 2009). *Drosophila* larval muscle growth correlates with the increasing sarcomere number (Haas, 1950). To quantify the magnitude of sarcomere addition during larval growth, we assessed the sarcomere number at different larval stages in two different muscles, VL1 (ventral longitudinal 1) and LT1 (lateral transverse 1), using a Zasp-GFP protein trap (Zasp::GFP) that marks the Z disc of sarcomeres. In both muscles, the number of sarcomeres increases by >100% from the 1st to the late 3rd-instar stage (Figure 1B). Furthermore, muscle length increased correspondingly, while sarcomere size remained constant (Figures 1C and 1D). In accordance with a consistent sarcomere size throughout larval development, cell length and sarcomere number revealed a precise linear scaling relationship (r = 0.98; Figures 1E and 1F). These data indicated that the *Drosophila* larval musculature provides an excellent system to study sarcomere addition and maintenance.

To investigate the role of *Dm*CFL in the larval musculature, we used the *Gal4/UAS* system to manipulate protein levels specifically in the muscle cells (Brand and Perrimon, 1993). Using an early embryonic muscle driver, *Dmef2-Gal4,* we expressed two different *UAS-RNAi* (RNA interference) constructs, referred to as *DmCFL RNAi (1)* and *DmCFL RNAi (2)* (Figure S1A). When expressing either RNAi, phenotypes were first observed at the 2nd-instar stage. These included a severe disruption of muscle fiber structure and sarcomere organization and early death (Figures S1B–S1D). Expression of wild-type *Dm*CLF

Author Manuscript Author Manuscript Author Manuscript Author Manuscript

(*DmCFL*^{WT}), together with either of the *DmCFL RNAi* constructs, rescued muscle and sarcomere structures and viability (Figures S1B–S1D). We expressed *2x-GFP* together with *DmCFL RNAi (1)* as a control for Gal4 dilution and found no change in viability, compared to the expression of *DmCFL RNAi* alone (Figure S1E). These experiments showed that targeted knockdown of *DmCFL* using a strong, early embryonic driver caused severe muscle phenotypes; however, the early larval death impeded detailed analyses of the role of *Dm*CFL in sarcomere organization and in muscle growth and function.

To bypass this early larval lethality, we expressed each *DmCFL RNAi* construct with the muscle Gal4 line, *Mhc-Gal4,* that drives expression later in embryogenesis and at lower levels relative to *Dmef2-Gal4* (Kaya-Çopur and Schnorrer, 2019; Viswanathan et al., 2015; Zhang and Bernstein, 2001). At the 3rd-instar stage, *DmCFL RNAi (1)* expressing larvae showed slower locomotion, disrupted muscle structure with Zasp-containing aggregates, and death after the larval stages (Figures 1G, 1H, and S1F). The expression of *DmCFL*^{WT} together with *DmCFL RNAi (1)* rescued viability and muscle structure, while the expression of *2x-GFP* together with *DmCFL RNAi (1)* failed to improve viability (Figures 1H and S1F-S1H). Expression of *DmCFL RNAi (2*) with *Mhc-Gal4* did not cause any obvious muscle phenotypes or viability issues due to insufficient *Dm*CFL knockdown (Figures 1H, S1F, S1G, and S1I).

Consistent with an effect of the loss of *Dm*CFL on sarcomere structure, we found that *Dm*CFL protein was localized specifically to the Z disc and the H zone of sarcomeres (Figures 1I, 1J, and S1J). This expression was lost upon *Dm*CFL knockdown (Figure S1I). In accordance with these imaging results, immunoblotting of the whole 3rd-instar larvae revealed a 60% reduction in *Dm*CFL levels (Figures S1K and S1L). These data demonstrated that in using a specific combination of genetic tools (*Mhc-Gal4*, *UAS DmCFL RNAi (1)*), we developed a *Drosophila* model for the detailed analysis of sarcomeric organization during muscle growth.

*Dm*CFL Knockdown Results in Three Classes of Muscle Phenotypes

To further investigate the structural changes within the muscle fibers at the 3rd-instar stage, we examined the organization of Z discs (Zasp) and thin filaments (F-actin) in detail. *Dm*CFL-knockdown larvae exhibited a range of muscle phenotypes. Individual muscles within the same larval hemisegment were differentially affected (Figure 2A). We identified three muscle classes based on the extent of structural disruption (Figure 2B). Class 1 muscles (65.875% ± 3.76%) resembled control muscles, as both Zasp and F-actin retain their sarcomeric organization throughout the fiber. Class 2 muscles (6.633% ± 0.074%) displayed dense F-actin accumulations at the fiber poles, although Zasp maintained normal sarcomeric organization. Class 3 muscles (27.492% ± 3.69%) showed a complete disorganization of F-actin and Zasp (Figure 2C). Our detailed analysis revealed a range of muscle phenotypes in the 3rd-instar *Dm*CFL-knockdown larvae; moreover, the most severely affected muscles contained protein aggregates at different positions throughout the muscle fibers.

Protein aggregates called nemaline bodies are the diagnostic feature of NM and contain Z disc proteins such as α-actinin, along with other sarcomeric proteins, including actin,

Author Manuscript Author Manuscript Author Manuscript Author Manuscript

tropomyosin, and nebulin (Agrawal et al., 2004, 2007; Ilkovski et al., 2001; Sewry et al., 2019). Nemaline bodies diffusely distribute in the cytoplasm, cluster under the cell membrane, localize near nuclei, or are found in lines within muscle fibers (Sewry et al., 2019). An examination of the protein aggregates found in our *Dm*CFL-knockdown muscles revealed F-actin and α-actinin co-localization (Figure 2D). Moreover, we observed co-localization of the F-actin with other components of the Z disc (e.g., kettin; Figure 2E). We further examined larval muscle ultrastructure by transmission electron microscopy (TEM). In class 3 *Dm*CFL-knockdown muscles, we observed a severe disruption in the sarcomeric pattern and the presence of protein aggregates near the muscle periphery (Figures 2F and 2G). Unlike the classical electron-dense, rod-like nemaline bodies seen in NM patients (Agrawal et al., 2007; Malfatti et al., 2014), the protein aggregates found in *Dm*CFL-knockdown muscles were mostly composed of actin. The lack of electron-dense material, however, may be due to the larval Z discs not being as electron dense as Z discs in adult *Drosophila* muscle or vertebrate muscle. These data indicated that muscle-specific knockdown of *Dm*CFL leads to sarcomeric degradation and to the formation of protein aggregates that shared some similarities to nemaline bodies seen in NM patients.

*Dm*CFL-Knockdown Muscles Show Progressive Deterioration

The structural changes in *Dm*CFL-knockdown muscles described thus far were observed in late 3rd-instar larvae at the end of larval development. To determine whether *Dm*CFL was required for initial sarcomere assembly in the embryo or for sarcomere maintenance, which occurs during the larval stages, we examined sarcomere formation in the *DmCFL* null mutant $DmCFL^{N96A}$. The $DmCFL^{N96A}$ homozygous mutant embryos have muscle defects, including missing muscles (Figure S2A). However, in the muscles that are present, sarcomeres are formed by stage 17, similar to control (Figure S2B), suggesting that *Dm*CFL is not required for embryonic sarcomere assembly. To examine the onset of the phenotypes observed when *Dm*CFL is reduced specifically in the muscles, we analyzed sarcomere organization each day over the 5-day larval period (Figure 3A). At the end of embryonic development (stage 17), we did not detect significant differences between *Dm*CFL knockdown and controls, which is consistent with the observation in $DmCFL^{N96A}$ embryos. *Dm*CFL-knockdown larvae showed sarcomere perturbations starting at the 2nd-instar stage, which increased throughout the 3rd-instar stage (Figure 3A). This loss in sarcomere organization was accompanied by a steady decline in muscle function, as measured by larval crawling velocity, starting at the 2nd-instar stage (Figure 3B). We concluded that while functioning muscles are initially established, the breakdown of sarcomere structure and muscle function is progressive and occurs in parallel over several days of *Dm*CFL knockdown.

To further probe the link between the deterioration of muscle structure and muscle function, we analyzed the locomotive performance and the distribution of muscle classes in individual *Dm*CFL-knockdown larvae. At the early 3rd-instar stage, the *Dm*CFL-knockdown larvae as a group had a higher percentage of class 2 and class 3 muscles and a lower percentage of class 1 muscles (class 1: 65.87% ± 3.76%, class 2: 6.63% ± 0.07%, class 3: 27.49% ± 3.69%) in comparison to control larvae (Figure 3C). We also assessed the muscle structure in individual *DmCFL RNAi (1)* larvae, with clearly distinct crawling velocities (Figure 3D). A

Author Manuscript Author Manuscript Author Manuscript Author Manuscript

larva that exhibited a higher locomotion velocity (top of the spread) had a higher percentage of class 1 (90%) and a lower percentage of class 3 muscles (5%), while a larva with a lower locomotion velocity at the bottom of the spread had a lower percentage of class 1 (29%) and a higher percentage of class 3 (65%) muscles (Figure 3D). As expected, a larva in the middle of the range had class 1 (68%) and class 3 muscles (25%) between that of the top and bottom (Figure 3D). These data supported a direct correlation between defective muscle structure and impaired muscle function.

To confirm that the muscle classes that we identified represent different stages in the progression of *Dm*CFL-dependent muscle deterioration, we imaged the musculature of the same individual larvae each day during larval development. These analyses reinforced that individual fibers that started out as class 1 muscles progressed to class 2 and culminated as class 3 (Figure 3E). No *Dm*CFL protein was detected in either class 2 or class 3 muscle cells by immunofluorescence, suggesting that this progression was not the result of a sudden depletion of *Dm*CFL at this stage (Figure S2C). Quantification of the different muscle classes (Figures 3F and S2D) further established a progressive increase in the number of class 2 and 3 muscles with successive larval stages.

These data suggested that the progressive deterioration of *Dm*CFL-knockdown muscle fibers follows a specific pattern of structural changes of sarcomeric proteins that directly correlates with locomotive performance.

F-Actin Aggregates Recruit Sarcomeric Tropomodulin and Troponin

We next sought to understand the temporal sequence in which the sarcomeric structure deteriorates upon *Dm*CFL knockdown. To this end, we examined the localization of other sarcomeric proteins in the different classes of *Dm*CFL-knockdown muscle fibers. All of the proteins tested were correctly localized in class 1 muscle fibers and mislocalized in class 3 muscles, yet showed distinct patterns in class 2 muscles (Figures S3A–S3E, S4A, and S4B). Proteins that maintained their localization in class 2 muscle cells included the actin-regulating protein Lasp/Nebulin, the barbed end-binding protein Cpa/CapZ, the actin-polymerizing protein SALS, the myosin heavy chain (Mhc), and the M-line protein obscurin (Figures S3C–S3E, S4A, and S4B). In contrast, Tropomodulin (Tmod) and Troponin T (TnT), two proteins with capping function at the pointed end of actin filaments, showed aberrant patterns in class 2 muscle cells (Figures 4A and 4B). In control cells, Tmod localized in a repeated manner at the pointed ends of the sarcomeric actin filaments, while TnT localized along the length of the actin filaments (Figures 4C and 4E), as previously described (Farah and Reinach, 1995; Mardahl-Dumesnil and Fowler, 2001). In class 2 muscle cells, both Tmod and TnT co-localized with F-actin at the cell poles, and their levels were decreased in the muscle cell center (Figures 4C–4F). Overall, Tmod and TnT intensities within the entire class 2 muscle fibers were similar to controls (Figures S4C and S4D). These data suggested that in *Dm*CFL-knockdown muscle fibers, Tmod and TnT were not maintained in sarcomeres at the cell center and were instead recruited to the actin accumulations at the cell poles. Thus, in our *Dm*CFL-knockdown model, the ectopic accumulation of actin and the recruitment of pointed-end actin-capping proteins represent the first visible intracellular signs of sarcomere deterioration.

Author Manuscript Author Manuscript Author Manuscript Author Manuscript

*Dm*CFL-Knockdown Muscles Form F-Actin Aggregates Instead of New Sarcomeric F-Actin

The onset and progression of the phenotypes in *Dm*CFL-knockdown muscle cells coincide with a rapid growth phase of the musculature during the late 2nd- and early 3rd-instar stages (Figure 1). During this period, control muscles increased by 50% in both muscle cell length and sarcomere number, while a significant number of *Dm*CFL-knockdown muscles started accumulating F-actin at their poles (Figure 2). The poles of muscle fibers have long been thought to be sites of sarcomerogenesis in both skeletal muscle fibers and cardiomyocytes (Bai et al., 2007; Dix and Eisenberg, 1990; Haas, 1950; Yang et al., 2016). To determine whether *Dm*CFL knockdown affects sarcomere addition during muscle cell growth, we analyzed the number of sarcomeres (Zasp-GFP) in ventral longitudinal (VL) muscles in early 3rd-instar larvae (Figure 5A). In comparison to controls, both class 1 and class 2 muscles had significantly fewer Z discs (Figures 5B and S5A). This decrease in sarcomere number was accompanied by an increase in sarcomere length (Figure 5C), consistent with the role of cofilin in regulating actin filament length in cardiomyocytes (Kremneva et al., 2014).

To determine whether *Dm*CFL regulates actin filament addition specifically, we analyzed the number of F-actin bands in pairs of VL muscles, which have the same number of sarcomeres in controls (Figure 5D). Despite having the same number of Z discs (Figure 5A), class 2 muscles contained significantly fewer sarcomeric F-actin bands compared to their class 1 neighbors (Figures 5D–5F). To further understand this decrease, we examined both Z disc and F-actin structures at the muscle poles (Figure 5G). In control and class 1 muscles, F-actin and Zasp co-localize in a sarcomeric pattern. In class 2 muscles, Zasp was organized in bands at the poles, while the F-actin filaments were not arranged in a periodic pattern (Figure 5G). At the poles of the class 2 muscles, the Z discs appeared to be crosslinked by long actin filaments that are different sizes and disarrayed, instead of actin filaments of a specific length. As these actin filaments did not resemble the actin bands seen in control sarcomeres in either length or shape, we did not count them as sarcomeric F-actin bands (Figure 5E). This suggested that in *Dm*CFL-knockdown muscles, F-actin forms accumulations at the cell poles, instead of precisely trimmed and organized thin filaments in newly formed sarcomeres.

These data suggest that *Dm*CFL plays two crucial roles in growing larval muscles. First, *Dm*CFL maintains the size of existing sarcomeres, possibly via regulation of sarcomeric F-actin length. Second, *Dm*CFL is necessary for the addition of F-actin in new sarcomeres at the cell poles.

Increased Proteasome Activity Improves *Dm*CFL-Knockdown Phenotypes

*Dm*CFL knockdown in the muscle fibers resulted in the presence of large sarcomeric protein aggregates and overall deterioration of muscle structure and function. We next asked why sarcomeric proteins accumulated instead of being degraded by the proteolytic machinery. Fluorescence recovery after photobleaching (FRAP) analysis revealed no significant difference in overall recovery rates of the Z disc protein, Zasp-GFP, in *control RNAi-* and *DmCFL RNAi (1)*-expressing muscle cells (Figures 6A and S6A). Furthermore, the levels of the mobile fractions of Zasp-GFP were similar (Figure 6B). These data suggested that the

Author Manuscript Author Manuscript Author Manuscript Author Manuscript

sarcomeric protein aggregates in the *Dm*CFL-knockdown muscle fibers, like the sarcomeres in control fibers, are dynamic structures with proteins rapidly binding and being released.

To investigate the possibility that the sarcomeric protein aggregates result from defective protein degradation, we analyzed protein degradation by the proteasome. As the proteasome targets and degrades ubiquitinated proteins, we examined whether mono- and poly-ubiquitination of the protein aggregates occurred. Immunoblotting of 3rd-instar larval carcasses revealed a significant increase in ubiquitinated protein levels in the *Dm*CFL-knockdown muscles compared to controls (Figures 6C and 6D). Analysis of the individual *Dm*CFL-knockdown muscles showed that the sarcomeric proteins in the aggregates were ubiquitinated and that overall ubiquitin levels were elevated in the class 3 muscle cells compared to controls (Figures 6E–6G). These data indicated that the aggregated proteins were properly targeted for degradation.

To test the ability of the muscle cells to degrade the ubiquitinated proteins, we overexpressed DmPI31, which increases proteasome activity (Bader et al., 2011). In control muscles, DmPI31 overexpression had no obvious effect on muscle structure, function, or viability of the organism (Figures S6B–S6E). Immunofluorescence images of the larval muscles expressing *DmPI31* with *DmCFL RNAi (1)* indicated that the localization of DmPI31 in both class 1 and 2 muscle cells was similar to that seen in controls (Figure S6B). However, co-expression of *DmPI31* with *DmCFL RNAi (1)* resulted in a significant improvement in muscle cell structure and function compared to the expression of *DmCFL RNAi (1)* alone (Figures 6H, 6I, and S6F). More important, the percentage of class 1 muscle cells was increased at the expense of class 3 muscles, indicating that the progressive changes to muscle structure were delayed by increasing proteasome activity.

To confirm this result, we inhibited proteasomal activity by expressing *DTS5*, a temperature-sensitive missense allele of the b6 subunit of the 20S proteasome, which inhibits proteasomal activity by acting as a dominant negative (Belote and Fortier, 2002). Embryos expressing these constructs were incubated at the restrictive temperature (29°C) throughout larval development. We observed no change in muscle cell structure and function upon *DTS5* expression in the control muscles (Figures S6D, S6G, and S6H). However, *DTS5* expression combined with *DmCFL RNAi (1)* caused accelerated muscle cell degeneration, with an increase in aberrant muscle structure (Figure 6J; class 3: 38.74% ± 0.72%). We did not detect any further worsening in larval locomotion velocity, which was already at a very low level. These data suggest that muscle cell degeneration was accelerated by inhibiting the proteasome (Figure 6I).

We expressed two copies of *UAS-GFP* along with *DmCFL RNAi (1)* as controls for these experiments and found that they did not improve larval muscle cell structure or function, indicating that Gal4 dilution does not contribute to improved muscle function seen in our rescue with *Dm*CFL (Figures 6K and 6L). In addition, the expression of *DmPI31* or *DTS5* in *DmCFL*-knockdown muscle cells did not affect the depletion of *Dm*CFL by *DmCFL RNAi (1)* and failed to improve the overall viability (Figures S6I and S6J).

Author Manuscript Author Manuscript Author Manuscript Author Manuscript

These results suggest that proteasome activation in our *Dm*CFL-knockdown model delays the progression of structural and functional muscle deterioration and the formation of protein aggregates.

NM Patient Point Mutation in CFL2 Abrogates CFL Function *In Vitro* and *In Vivo*

CFL2 mutations seen in NM patients include both small deletions and point mutations (Agrawal et al., 2007; Ockeloen et al., 2012; Ong et al., 2014). Our *Dm*CFL-knockdown models recapitulate some aspects of muscle cell degeneration observed in a severe case of human NM, in which a *CFL2* null mutation was detected (Ong et al., 2014). The muscle fibers of this patient showed nemaline bodies at the cell peripheries and reduced muscle function. Point mutations in *CFL2,* thought to be hypomorphs, have been identified in patients with less severe cases of NM. One of these point mutations alters a single amino acid p.Val7-Met (V7M), which is conserved between *Drosophila*, mouse, and human cofilins/Tsr (Figures 7A and S7A).To understand how the V7M mutation affects protein function, we biochemically compared the interactions and activities of human $CFL2^{WT}$ and $CFL2^{V7M}$. Analysis of the nucleotide exchange rate on actin monomers (ADP to ATP) revealed that the rate is increased in $CFL2^{V7M}$, suggesting that it has enhanced affinity for G-actin (Figure 7B). Furthermore, *in vitro* total internal reflection fluorescence (TIRF) microscopy analysis revealed that the ability of $CFL2^{V7M}$ to sever actin filaments is compromised, which is evident from its reduced plateau of cumulative severing compared to $CFL2^{WT}$ (Figures 7C, 7D, and S7B). Continuous actin turnover is critical for maintaining sarcomere structure and muscle function (Ono, 2010). Our experiments showed that the V7M mutation in CFL2 severely compromises the functional interactions of CFL2, by increasing the levels of ATP-actin monomers and decreasing the F-actin severing rate.

To test the effects of the V7M mutation in *Drosophila* muscles, we engineered constructs expressing *DmCFL* and human *CFLs* containing the mutation (Figures 7A and S7A). *Dm*CFL^{WT} and *Dm*CFL^{V7M} localize to sarcomere Z discs and H zones, similar to endogenous *Dm*CFL in control muscle fibers (Figures S7C–S7F, compare to Figure 1I). While the expression of $DmCFL^{WT}$ in *DmCFL*-knockdown muscles rescued muscle function, structure, and viability, the expression of $DmCFL^{V7M}$ did not rescue wild-type *Dm*CFL function (Figures 7E, 7F, and S7G). The expression levels of both constructs were confirmed through western analysis (Figures S7H and S7I), suggesting that, like human $CFL2^{V7M}$, *Dm*CFL^{V7M} is a hypomorph.

To test the function of human CFL proteins in our *Drosophila* model, we expressed $CFL2^{WT}$, $CFL2^{V7M}$, and $CFL1^{WT}$ in *Dm*CFL-knockdown larval muscle cells. We used the strong muscle GAL4 driver, *Dmef2-Gal4,* and expressed two copies of each of the constructs. We confirmed the expression levels of all constructs through western blots (Figures S8A and S8B) and found that the proteins encoded by $CFL2^{V7M}$, $CFL2^{WT}$, and $CFL1^{WT}$ localized to the *Drosophila* sarcomere Z -disc and H-zones, similar to the fly protein (Figures S8C–S8H; compare Figure 1I). Co-expression with *DmCFL RNAi (1)* showed that $CFL2^{WT}$ improved muscle cell structure and function similar to *Dm*CFL (Figures 7G–7I and S8I), indicating that the human and *Drosophila* proteins have similar function in muscle cells. Expression of $CFL2^{V7M}$ also showed some rescue of both muscle

Author Manuscript Author Manuscript Author Manuscript Author Manuscript

cell structure and function, but not to the same extent (Figures 7G–7I and S8I). We hypothesized that this rescue by CFL2^{V7M} can be attributed to the mutant protein's retaining some function *in vivo*, as was seen our *in vitro* experiments (Figures 7B–7D). The expression of *CFL1*^{WT} in *Dm*CFL-knockdown muscle cells also rescued muscle cell structure and function (Figures 7G–7I and S8I), as *Dm*CFL and both human CFLs, CFL1 and CFL2, share 37% protein sequence homology (Figure S7A). The slightly better rescue with *CFL1*^{WT}, compared to that with *CFL2*^{WT}, can be attributed to the higher expression level (Figure S8B). As a control for these experiments, the expression of two copies of *UAS-GFP* along with *DmCFL RNAi (1)* did not improve larval muscle cell function (Figure 7I), indicating that Gal4 dilution is not contributing to the improved muscle function seen in our rescue with the human CFLs.

These data show functional similarities between human and fly CFL proteins and indicate that the human V7M mutation impairs the ability of CFL2 to sever actin filaments both *in vivo* and *in vitro*.

DISCUSSION

The roles of CFLs have been studied in a variety of systems. Both *in vivo* and *in vitro* studies have suggested that CFL2 localizes to existing sarcomeres and is required, via its actin-severing activity, for maintaining F-actin length and sarcomere structure (Andrianantoandro and Pollard, 2006; Gurniak et al., 2014; Kremneva et al., 2014; Michelot et al., 2007; Ono et al., 2003). We show that *Dm*CFL specifically localizes to both the Z disc and H zone in larval sarcomeres and that muscle-specific knockdown of *Dm*CFL affects existing sarcomere length. In severely affected *Dm*CFL-knockdown muscles, we find a complete collapse of sarcomere organization and the formation of actin aggregates, similar to previous studies investigating the loss of CFL2 or its homologs (Agrawal et al., 2012; Gurniak et al., 2014; Ono et al., 1999, 2003; Subramanian et al., 2015). Our work also uncovers the role of CFL in sarcomerogenesis during muscle growth, an area that has not been studied previously. The *Drosophila* larval muscles grow 25- to 40-fold in size over a period of 5 days, which parallels an increase in sarcomere number (Demontis and Perrimon, 2009; this study, Figure 1). The loss of *Dm*CFL disrupts sarcomeric F-actin addition in growing muscle cells, resulting in F-actin accumulations at the poles coupled with fewer sarcomeres. Previous TEM and time-lapse imaging data suggest that the ends of the myofibers are the sites of sarcomerogenesis (Dix and Eisenberg, 1990; Yang et al., 2016). Moreover, the F-actin accumulations at muscle cell poles have been previously observed in zebrafish models of NM (Sztal et al., 2015). While existing studies support our suggestion that the loss of *Dm*CFL leads to the accumulation of F-actin specifically in regions of sarcomere addition, future studies involving pulse chase experiments with fluorescently tagged sarcomeric proteins need to be performed to confirm our hypothesis. Alternatively, the F-actin accumulations at the poles could suggest an increased susceptibility of the sarcomeres at the poles to CFL depletion, resulting in the excessive polymerization of F-actin at the muscle poles and subsequent aggregate formation. This alternative remains to be tested in future studies.

Author Manuscript Author Manuscript Author Manuscript Author Manuscript

Our *Dm*CFL-knockdown model showed that the deterioration of muscle structure and function was progressive in nature and occurred in parallel. Initially, all *Dm*CFL-knockdown muscles had control features (class 1). These observations are similar to *Cfl2*-knockout mouse models, in which CFL2 is not necessary for initial myofibrillogenesis, but is required for subsequent muscle development (Agrawal et al., 2012; Gurniak et al., 2014). However, it is possible that the appearance of muscle phenotypes in the 3rd-instar larval stages and not earlier is due to the insufficient knockdown of *Dm*CFL by *Mhc-Gal4*, as class 1 muscles still retain *Dm*CFL expression in their muscles. On a cellular level, the decline in muscle function in the *Dm*CFL-knockdown larvae can be attributed to several factors. First, sarcomere sizes increase concomitantly with fewer sarcomeric F-actin filaments being added to the growing muscle, which results in a weaker muscle with lower force production. Second, the formation of actin aggregates at the cell poles (class 2 muscles), most likely a result of unchecked actin polymerization, interferes with muscle contraction. Third, the F-actin aggregates recruit Tmod and TnT, actin-capping proteins, leading to a reduction in the levels of these proteins at existing sarcomeres, which likely promotes their destabilization. The loss of Tmod and TnT from sarcomeres has been shown to result in reduced muscle function (Nworu et al., 2015; Singh et al., 2014; Stevenson et al., 2007). Furthermore, the mislocalization of Tmod has been shown in a *Drosophila* model overexpressing *ACTA1* mutation seen in NM patients (Sevdali et al., 2013). Future experiments will need to further address whether Tmod and TnT are recruited to the F-actin aggregates from existing sarcomeres or from the pools of newly synthesized Tmod and TnT proteins. In the absence of CFL2, capping proteins bind and regulate actin filament length less efficiently (Fowler, 1996; Kremneva et al., 2014). Thus, it is likely that the suboptimal capacity of these capping proteins, in combination with loss of *Dm*CFL, ultimately leads to the collapse of sarcomeric organization (class 3 muscles), thereby significantly impairing muscle contraction and locomotion.

Sarcomeric proteins undergo rapid turnover (Littlefield and Fowler, 2008; Sanger and Sanger, 2008; this study, Figure 6), which requires high levels of protein production and degradation. We investigated why aggregated sarcomeric proteins were not degraded by the proteasome in our *Dm*CFL-knockdown model and found that the aggregates were in constant flux and properly targeted for ubiquitination. Furthermore, we showed that upon proteasome overactivation, muscle deterioration was slowed down but not completely eliminated. These data suggested that the proteasome was unable to compensate and process the unsevered F-actin. While other severing proteins such as gelsolin are expressed in the *Drosophila* muscle, they appear unable to compensate for the loss of *Dm*CFL. These data further highlight the importance of *Dm*CFL in sarcomere addition and homeostasis and provide crucial insights to the mechanisms underlying the formation of sarcomeric protein aggregates, as well as possible therapeutic approaches. In addition to the proteasome, upregulation of the autophagy pathway through the mammalian target of rapamycin (mTOR) has been shown to reduce the levels of mutant proteins and improve disease progression in both *Drosophila* and mice models of aggregate diseases such as Huntington disease, and spinocerebellar ataxia type 3 (SCA3) (Berger et al., 2006; Ravikumar et al., 2002, 2004). Similarly, *Cfl2*$^{-/-}$ mice show an upregulation of the autophagy pathway in their muscle (Gurniak et al., 2014). This suggests that manipulating autophagy would also help clear the

Author Manuscript Author Manuscript Author Manuscript Author Manuscript

protein aggregates in our *Dm*CFL-depleted muscles. Specifically, the breakdown of sarcomeric protein aggregates and the recycling of limiting components such as actin could improve muscle contraction and locomotion.

NM is a slowly progressing myopathy characterized by muscle weakness and the presence of nemaline bodies containing both actin and α-actinin (Sewry et al., 2019). Mutations in CFL2 have been identified in three isolated cases of NM (Agrawal et al., 2007; Ockeloen et al., 2012; Ong et al., 2014). Mouse models of *Cfl2* recapitulate aspects of the disease such as the degeneration of muscle fibers, the presence of actin and α-actinin^{+} nemaline bodies, sarcomeric disruptions, actin accumulations, and muscle weakness (Agrawal et al., 2012; Gurniak et al., 2014). In our *Dm*CFL-knockdown *Drosophila* muscles, we see disruption of both muscle and sarcomere structure and loss of muscle function. These phenotypes can be rescued with the human CFL genes, indicating strong conservation between the *Drosophila* and human proteins. While the protein aggregates in our *Dm*CFL-knockdown muscle fibers do not completely mimic the electron-dense nemaline bodies seen in NM patients, they do have similar protein compositions (F-actin and α-actinin) and subsarcolemmal localization (Sewry et al., 2019). Similar to NM patients and *Cfl2* mouse models, not all muscle fibers in our *Dm*CFL-knockdown larvae are affected and deteriorate at the same time and rate (Agrawal et al., 2012; Gurniak et al., 2014). Our data show that the timing and strength of RNAi expression correlate with the timing and severity of structural changes, indicating that protein levels play a crucial role in the onset and progression of phenotypes. Furthermore, we strongly implicate muscle growth as a factor in the progression of muscle phenotypes. Mammalian muscle grows dramatically in size postnatally and during puberty (Bachman et al., 2018; Lexell et al., 1992; Pearson, 1990). The postnatal period of muscle growth correlates with the transition from the expression of *CFL1* and *ADF* to *CFL2* genes (Abe and Obinata, 1989; Abe et al., 1989; Bamburg and Bray, 1987; Gurniak et al., 2014). The expression of CFL2 as the predominant isoform in the skeletal muscle (Thirion et al., 2001) and the demand for increased sarcomerogenesis suggest that muscle growth could contribute to NM disease onset and progression. Accordingly, NM symptoms have been known to develop during the prepubertal growth spurt (Sanoudou and Beggs, 2001). Using our *Drosophila* model to test whether factors such as growth and activity modulate the muscle phenotypes remains a goal.

In summary, our data implicate specific roles for CFLs in sarcomere addition and maintenance through the regulation of actin thin filaments. We propose a model for nemaline body formation that rests on the fundamental structure and organization of the sarcomere: aberrant accumulation of one sarcomeric component in the muscle cell nucleates the subsequent recruitment of addition sarcomeric components from existing sarcomeres and/or newly made proteins to the sites of accumulation. Similar mechanisms could lead to the formation of nemaline bodies found in patients. Our results describing how the NM point mutations affect the function of CFL2 will aid in screening for therapeutics to improve muscle function in these NM patients. Future analyses could shed light on the contribution of muscle type, metabolism, and other pathways to the progression of the structural changes within the muscle.

Author Manuscript Author Manuscript Author Manuscript Author Manuscript

STAR★METHODS

RESOURCE AVAILABILITY

Lead Contact—Further information and requests for resources and reagents should be directed to and will be fulfilled by the Lead Contact, Mary Baylies (m-baylies@ski.mskcc.org).

Materials Availability—Fly lines generated in this study are available from the Lead Contact without any restriction.

Data and Code Availability—This study did not generate or analyze datasets or code.

EXPERIMENTAL MODEL AND SUBJECT DETAILS

Drosophila stocks and crosses were grown on standard cornmeal medium at 25°C in 12:12 Light:Dark conditions under constant humidity. For experiments using *DTS5*, flies were raised at 25°C and then shifted to the permissive temperature, 29°C, to activate DTS5 function. tsr^{N96A} (BDSC #9108), null mutant, was used to examine sarcomere formation. The *GAL4-UAS* system (Brand and Perrimon, 1993) was used for expression studies. For muscle-specific expression, *Dmef2-Gal4* (Halfon et al., 2000), and *Mhc-Gal4* (BDSC# 67044) were used. *UAS-mCherry-RNAi* (BDSC# 35785) was used as the *control RNAi. UAS-tsr-RNAi (HMS00534)* (BDSC #65055) was used as *tsr RNAi (1). UAS-tsr-IR* (VDRC #110599) was used as *tsr RNAi (2). UAS-HA-PI31* (Bader et al., 2011) and *UAS-DTS5* (Bader et al., 2011) were used to manipulate the proteasome (gift of H. Stellar). *UAS-2x-GFP* (BDSC # 6874) and *UAS-moesin::mCherry* (Millard and Martin, 2008) were used to outline the muscle to count sarcomeres. The following gene traps were used: *tsr::GFP (ZCL2393)* (DGRC #110875), *Tmod::GFP* (BDSC #50861), and *Zasp66::GFP (ZCL0663)* (BDSC #6824). Homozygous *tsr::GFP* (*ZCL2393*) flies are embryonically lethal and hence were only used in a heterozygous manner.

METHOD DETAILS

Viability assays—Embryos were collected at 25°C on yeasted apple juice agar plates. Stage 15–16 embryos lacking the balancer (where applicable) were staged by gut morphology and hand-selected for analysis. 35 embryos were counted and transferred to a lightly yeasted apple juice agar plate and raised at 25°C overnight. The first instar larvae that hatched the following day were counted and transferred to vials of standard fly food at 25°C. The above process was repeated for 3 days. Eight to ten days later, the number of pupal cases and adults present in the vials were quantified. For each genotype the experiments were repeated twice. For the *DmCFL RNAi (1)* alone the viability experiments were repeated three times and the same values were used throughout the paper in all the graphs containing *DmCFL RNAi (1)* driven by *Mhc-Gal4*. The mean survival along with SEM from the experiments were plotted using GraphPad Prism.

Transgenics—For the *Drosophila* $DmCFL^{WT}$ rescue experiments, $DmCFL^{WT}$ was PCR-amplified from EST clone LD06785 (*DGRC**) using the following primers: EcoRI-wt-tsr Forward: 5′-CACCGAATTCATGGCTTCTGGTGTAACTGTGTCT-3′ and BglII-tsr-

Author Manuscript Author Manuscript Author Manuscript Author Manuscript

noSTOP Reverse: 5′-CACCGAATTCATGGCTTCTGGTGTAACTATGTCTGATGTCTGCAAGACTACAT-3′. *DmCFL*^{V7M} was PCR-amplified from the same EST with nucleotide 19 mutated from G to A during that amplification using the following primer EcoRI-tsr-G19A Forward: 5′-CACCGAATTCATGGCTTCTGGTGTAACTATG TCTGATGTCTGCAAGACTACAT-3′ and the BglII-tsr-noSTOP Reverse primer.

The amplified products were cloned into the pENTR plasmid containing UASp and 3xHA (Life Technologies, cat# K240020), digested with EcoRI and BglII, and then ligated into pTWH (*DGRC**, cat# 1100). All constructs were sequenced and verified constructs were injected into w^{1118} embryos by transposable-p-element-based insertion methods (*Genetic Services*, Boston). Potential transformants were screened for w^{+}.

For human Cofilin rescue experiments, *CFL2*^{WT} was PCR-amplified from pET15b-CFL2 (Chin et al., 2016) using the following primers: EcoRI-cof-tsr-wt Forward: 5′-CACCGAATTCATGGCTTCTGGAGTTACAGTGAAT-3′ and BamHI-cof2-noSTOP Reverse: 5′-GGATCCTAATGGTTTTCCTTCAAGTGAAACT-3′. *CFL2*^{V7M} was PCR-amplified from the same template, using a forward primer containing the desired mutation (nuc.19G > A): 5′-CACCGAATTCATGGCTTCTGGAGTTACAATGAATGATGAAGTCATCAAAG TTTTT-3′ and the BglII-Cof2-noSTOP Reverse primer. *CFL1*^{WT} *was* PCR-amplified from pET15b-CFL1 (Chin et al., 2016) using the following primers: EcoRI-CFL1-wt Forward: 5′-CACCGAATTCATGGCCTCCGGTGTGGCTGTCT-3′ and BamHI-CFL1-noSTOP Reverse: 5′- GGATCCCAAAGGCTTGCCCTCCAGGGAG-3′.

The amplified products were cloned into the pENTR plasmid (Life Technologies, Cat#K240020), digested with EcoRI and BamHI, and then ligated into pUASg-3xHA.attB (gift from Konrad Basler, Univ. of Zurich). Constructs were injected in a site-directed fashion into attP40 (chromosome 2) and attP2 (chromosome 3) sites of w^{1118} fly embryos (Rainbow Genetics). Transformants were screened for w^{+}.

Sequence Alignments—Protein sequence alignments were performed using MacVector 14.5.3.

Immunostainings—Stage 15–16 embryos of the respective genotype were hand-selected and grown at 25°C for 5 days until they reached 3rd instar. *DTS5-HA* flies were raised at 25°C and hand-selected, after which the first instar larvae were moved to 29°C and allowed to grow for 3 days until the larvae reached 3rd instar. Larvae were dissected in ice cold HL3.1 as described (Brent et al., 2009) and fixed with 10% formalin (Sigma, #HT501128–4L) for 20 minutes. Larval fillets were blocked with PBS supplemented with 0.1% BSA and 0.3% Triton X-100 for 30 minutes. Larval fillets were incubated with primary antibody overnight at 4°C, followed by washes in PBT-BSA and 2-hour incubation with secondary antibodies and Phalloidin at room temperature. After washes in PBT, larval fillets were then mounted in ProLong Gold (Invitrogen, #P36930). Z stacks were acquired using either a SP5 (Leica) laser-scanning microscope with 40x/1.25NA HCX PL Apochromat oil objective or an inverted LSM-700 (Zeiss) laser-scanning confocal microscope with either a Plan-

Author Manuscript Author Manuscript Author Manuscript Author Manuscript

Neofluor 5x /0.16 NA, 10x/0.30NA, 20x/0.8NA air objective or a 40x/1.4NA, 63x/1.4 DiC Apochromat oil objective. Maximum intensity projections of confocal Z stacks were rendered using Fiji (NIH). All resulting 2D projection images were cropped using Adobe Photoshop. Approximately 8 larvae of each genotype were dissected and a minimum of 3 different images for each muscle class was acquired. The most representative image was included as a Figure.

The following primary antibodies were used at the specified concentration: mouse anti-Myosin Heavy Chain (1:250), chicken anti-GFP(1:200), rabbit anti-Zasp (1:400), rabbit anti-Lasp (1:400), rat anti-Tropomodulin (1:200), rat anti–α-actinin (1:200), rabbit anti-Obscurin (1:200), rabbit anti-Cpa (1:200), rat anti-HA (1:100), rabbit anti-SALS (1:200), mouse anti-FK2 (1:200), rat anti-Troponin-T (1:200,) and rat anti-Kettin (1:200). Alexa Fluor 488-, 555-, and 647-conjugated fluorescent secondary antibodies (1:200), Alexa Fluor 488-, 546-, and 647-conjugated Phalloidin (1:100), to label F-actin, and Hoechst-3342 (1 mg/mL, Invitrogen), to label nuclei, were used for fluorescent stains.

Line profiles for protein localization—Immunofluorescent images of larval muscles were acquired using an inverted LSM-700 (Zeiss) laser-scanning confocal microscope with a 63x/1.4NA DiC Apochromat oil objective. Images were then analyzed using Fiji (NIH) where projections lines were drawn on single slice, spanning the length of 4 sarcomeres (Z disc- Z-disc) using Zasp staining. Fluorescence intensity along the lines were calculated using the Plot Profile function in Fiji (NIH). Intensity was normalized at every point along the line by using the formula: Relative fluorescence intensity = $\text{Intensity}_{\text{at point}} - \text{Intensity}_{\text{minimum}} / \text{Intensity}_{\text{maximum}} \times 100$. A maximum of 3 lines were drawn per muscle and at least 5 different muscles from 5 different larvae were analyzed. The relative fluorescent intensities of each channel were plotted on Graph Pad Prism, to generate line profiles for protein localization.

Larval tracking A larva was placed at the center of 8.5 cm apple juice agar plate. 45 s movies of the larva crawling were captured on an iPhone v.6.0. Movies were converted into image sequences and uploaded onto Fiji (NIH). Each larva was manually tracked using the Manual Tracking plugin on Fiji (NIH). Average velocity was calculated by averaging velocities of the larvae over 44 frames. Approximately 8 larvae of each genotype were tracked. Genotypes were compared by Student's t test in GraphPad Prism software.

For measuring larval velocities over different developmental stages, stage 15–16 embryos of the appropriate genotype were selected and allowed to develop at 25°C. The velocities of the larvae were determined every 24 hours, starting at the first instar stage. After tracking, the larvae were returned to the food. Approximately 8 larvae of each genotype were tracked. Velocities at different developmental stages were compared to the control larvae using ANOVA in GraphPad Prism software.

Western Blot Analysis—Larval pelts for immunoblotting were generated by dissecting larva as discussed above, followed by excision of the head and tail of the larva. The remaining muscle-enriched pelts were then transferred into Larval lysis Buffer (50mM HEPES, pH 7.5, 150mM NACl, 0.5% NP40, 0.1% SDS, 2mM DTT, 1 protease inhibitor

Author Manuscript Author Manuscript Author Manuscript Author Manuscript

cocktail tablets [1 tablet in 10mL of lysis buffer, Roche (#11836153001)]. Lysates were homogenized, and protein concentrations were determined using Bradford assay. Equal concentrations of protein (12.5 μg for Tsr:GFP and 40 μg for HA) were run on an either a 10% (for GFP), or a 12.5% (for HA) polyacrylamide gel after which they were transferred onto a nitrocellulose membrane (ThermoScientific, # 88018). Membranes were blocked with 5% milk in TBST (Tris-Buffered Saline +0.1% Tween) for an hour. The blots were then incubated with primary antibodies in 5% milk overnight at 4°C, and then for an hour at room temperature with secondary antibodies in 5% milk. The immunoreaction was visualized in a KwikQuant Imager (Kindle Biosciences, LLC, # D1001) using 1-Shot Digital-ECL (Kindle Biosciences, # R1003). Images were quantified using Fiji (NIH). Images were then processed using Adobe Photoshop. Figures and quantifications are representative of 3 biological replicates and protein expression was normalized GAPDH within each sample.

The following primary antibodies were used in the specified concentrations: mouse anti-GFP (1:1000), rat anti-HA (1:1000) and mouse anti-GAPDH (1:10,000). Peroxidase-conjugated donkey anti-mouse (1:5000) and Peroxidase-conjugated donkey anti-rat (1:5000, Jackson Immunoresearch) were used as secondary antibodies.

Electron microscopy—Third instar larvae were dissected as described previously and were immediately placed in fixative composed of 2% glutaraldehyde, 4% Paraformaldehyde, 2mM $Cacl_2$, 0.1% tannic acid in 0.1M sodium cacodylate buffer, pH 7.4. The samples were then fixed for 3 minutes using the Pelco Biowave (Ted Pella), followed by overnight fixation at 4°C. Samples were post-fixed with 1% osmium tetroxide containing 1.5% potassium ferrocyanide in cacodylate buffer for 1 hour on ice. They were then stained with 1% uranyl acetate aqueous solution for 30 minutes at room temperature. The samples were dehydrated in a graded series of ethanol using the Pelco Biowave and acetone dehydration at room temperature for 10 minutes. Samples were infiltrated and embedded with Eponate 12 (Ted Pella). 60–70nm ultrathin sections were then sectioned from 3 samples for each genotype using a Reichert Jung Ultracut E microtome. Sections were stained with 2% Uranyl acetate and Sato's lead stain and then imaged using a JEOL 1400 Plus Transmission Electron Microscope at 120kV equipped with a Gatan Ultrascan 994 US 1000XP camera and Digital Micrograph imaging software (a gift from Helmsley Charitable Trust) at the Electron Microscopy Resource Center in The Rockefeller University. For each genotype, approximately 3 biological replicates were processed and imaged. Images representative of each genotype are depicted in the Figures.

Larval heat fixation—Larvae of the appropriate stage containing RNAi and/or GFP protein trap were analyzed as previously (Windner et al., 2019). Stage 15–16 embryos were selected and developed at 25°C. Appropriately staged larvae were fixed by brief (~1 s.) submersion in 65°C water and then mounted on a slide with halocarbon oil. Images were acquired using an inverted LSM-700 (Zeiss) laser-scanning confocal microscope with either a 10x/0.30NA, 20x/0.8NA air-objective. Maximum intensity projections of confocal Z stacks were rendered using Fiii (NIH). All resulting 2D projection images were cropped using Adobe Photoshop. For analyzing *Dm*CFL::GFP levels in *control RNAi* and *DmCFL RNAi*

Author Manuscript Author Manuscript Author Manuscript Author Manuscript

(1) larvae at different developmental stages, images were acquired on the same day using identical laser power and software settings.

Time-lapse live imaging—Larvae were anesthetized as described in Choi et al. (2014). After selecting stage 15–16 embryos of the appropriate genotype, the larvae were imaged every 24 hours from first instar onward for 4 days. For imaging, larvae were placed on a slide with 50% glycerol and coverslip. Imaging time was limited to less than 20 minutes after which animals were washed gently with PBS, allowed to recover and returned to the food media. Images were acquired in an inverted LSM-700 (Zeiss) laser-scanning confocal microscope using the 10x/0.30NA air-objective. Maximum intensity projections of confocal Z stacks were rendered using Fiii (NIH). All resulting 2D projection images were cropped using Adobe Photoshop. Approximately 3 larvae of each genotype were tracked, the most representative images were included as Figures.

Fluorescence Recovery After Photobleaching (FRAP)—*Mhc-Gal4, Zasp66::GFP* female flies were crossed to control *RNAi* or *DmCFL RNAi (1)* males. Stage 15–16 embryos were collected on apple juice- agar plates and allowed to develop for 4 days at 25°C. Third instar larvae of both genotypes were anesthetized as described (Fernandes and Schöck, 2014) by exposure for 15–20 minutes to Kwan Loong Oil (Haw Par Healthcare Ltd). Anesthetized larvae were covered in 50% glycerol and were then mounted on a glass slide with a coverslip. Heartbeat was verified before acquisition to ensure that the larvae were alive during the recording. 3 unique Regions of interest (ROIs) were selected in a single larval muscle and the Zasp66::GFP was bleached using the 488-nm laser. Fluorescence recovery of Zasp66::GFP was recorded for approximately 10 minutes with a 488-nm laser, imaging every 30 s. Intensity of laser was set to ensure that bleaching was not below 20%–30% of initial intensity. Three muscles from three different larvae were analyzed for each genotype. Data were analyzed using Leica Application Suite X (Leica), where the intensities of the bleached, unbleached and background regions were normalized to set the prebleach intensities close to one, in order compare data across experiments. 9 independent recovery (3 biological replicates), normalized datasets were analyzed using GraphPad Prism software. The fitted line was calculated by the software using the one-phase exponential equation. Mobile fraction for each genotype was calculated using the formula Mobile fraction (F_m)= F_∞/F_0. F_∞ is the fluorescence intensity after full recovery and F_0 is the fluorescence intensity before photobleaching. Images were acquired at room temperature with a Leica TCS SP5 II confocal microscope, using a 20x/0.75NA glycerol immersion objective.

Muscle classes quantification—Third instar larvae of the appropriate genotypes were dissected as described above. Larval muscles stained with phalloidin as well as with a Z-disc protein were visualized using the 20x air-objective of the LSM-700 confocal microscope to classify muscles into the 3 different classes. All 30 muscles from a hemisegment were scored as either class 1,2 or 3 muscle. Only hemisegments with all 30 intact muscles were scored. A maximum of 5 hemisegments were counted per larva and 30 hemisegments in total were counted per genotype. The percentage of muscles falling into each class was

Author Manuscript Author Manuscript Author Manuscript Author Manuscript

calculated for each genotype. The percentages of each muscle class were calculated per genotype and plotted in GraphPad Prism, to generate graphs.

For calculating the number of muscles of different classes at each larval instar, *Tmod::GFP,Mhc-Gal4* females were crossed to control *RNAi* or *DmCFL RNAi (1)* males. Stage 15–16 embryos were collected on apple juice- agar plates and allowed to develop for at 25°C. Larvae were heat fixed every 24 hours from the first instar stage for 4 days. A maximum of 3 hemisegments per larvae, and a total of 15 hemisgements were analyzed for each developmental stage. Data were analyzed as in preceding paragraph. The percentage of each class of muscle at every larval stage was calculated. The percentages of each muscle class were plotted in GraphPad Prism, to generate graphs.

FK2 intensity measurements—Images of VL3 and VL4 muscles from *control RNAi* and *DmCFL RNAi (1)* larvae were acquired under identical conditions using an inverted LSM-700 (Zeiss) with a 20x/0.8NA air-objective. Images were then analyzed using Fiji (NIH). First threshold intensities were set for each channel in the *control RNAi* muscles. Hoechst channel was converted to a binary image and was then subtracted from the FK2 channel, to calculate pixel intensity only in the sarcoplasm. Raw Integrated Intensity was calculated in the outlined area. Number of pixels of FK2 per mm^2 of muscle mass was calculated by dividing the Raw Integrated Intensity with the Muscle Area. Experiment was repeated twice and plotted on GraphPad Prism to generate a graph. P values were calculated using Student's unpaired t test.

Troponin T (TnT) and Tropomodulin (Tmod) intensity measurements in the muscle—Images of VL3 and VL4 muscles from *control RNAi* and *DmCFL RNAi (1)* larvae were acquired under identical conditions using an inverted LSM-700 (Zeiss) with a 20x/0.8NA air-objective. Images were then analyzed using Fiji (NIH). Threshold intensities were initially set for TnT and Tmod channels in the *control RNAi* muscles. The center of the muscle was estimated using line tool in Fiji (NIH) and box measuring 217×68 pixels was drawn. Raw integrated pixel intensity was calculated in the outlined area. For measuring intensities for the entire muscle, the same procedure was followed as above, after threshold intensities were set the entire muscle was outlined and the raw integrated pixel intensity was calculated in the outlined area. Integrated pixel intensity of TnT/Tmod per mm^2 of muscle mass at the center of the muscle/ entire muscle was calculated by dividing the Raw integrated pixel intensity by the area of the region measured. A minimum of 13 different Class 2 muscles from 8 different *DmCFL RNAi (1)* larvae were imaged and analyzed. Experiment was repeated twice and plotted on GraphPad Prism to generate a graph. P values were calculated using Student's unpaired t test.

Sarcomere analysis

Sarcomere number—Larvae of the appropriate stage containing *Zasp66::GFP (ZCL0663)* protein trap and *UAS-moesin::mCherry* driven by *Mhc-GAL4* were heatfixed as described above, and maximum intensity confocal Z stacks were acquired. A total of 15 hemisegments from at least 5 different larvae were counted. Two different muscles of different sizes were chosen (VL1 and LT1), and number of sarcomeres in each muscle was

Author Manuscript Author Manuscript Author Manuscript Author Manuscript

counted by counting number of Z-lines. Numbers were plotted in GraphPad Prism, to generate graphs.

Muscle length and Sarcomere size—Muscle length of the above muscles were calculated by using the line function on Fiji (NIH) to draw a line from one muscle end to the other. The muscle length was then divided by the number of sarcomeres to determine average sarcomere size for each muscle at each instar. Numbers were plotted in GraphPad Prism, to generate graphs. Pearson's correlation coefficient (r) and R^2 values were calculated using GraphPad Prism.

Sarcomere number in Class 1 and Class 2 muscles—Early 3rd instar larvae of the *Zasp66::GFP (ZCL0663)* protein trap and *UAS-moesin::mCherry* and either *UAS-mCherry RNAi/ UAS tsr TRiP RNAi* driven by *Mhc-GAL4* were heat fixed as described above, and maximum intensity confocal Z stacks were acquired. A total of 9 hemisegments from 5 different larvae containing one Class 1 VL muscle and a Class 2 were counted by counting number of moesin-mCherry or Zasp::GFP lines. Pearson's correlation coefficient (r) and R^2 values were calculated using GraphPad Prism. Number of sarcomeres were plotted against muscle length in GraphPad Prism, to generate graphs.

Plasmids and protein purification—The plasmid for *E. coli* expression of human Cof2 was a gift from Dr. David Kovar (University of Chicago). Site-directed mutagenesis was performed on this plasmid to introduce the V7M mutation, and the resulting plasmid was verified by DNA sequencing. Rabbit skeletal muscle actin was purified, and in some preparations labeled on Cys^{374} with Oregon Green maleimide (Life Technologies), as described in detail (Graziano et al., 2013). Human $CFL2^{WT}$ and $Cof2^{V7M}$ were purified from *E. coli* as described (Chin et al., 2016). In brief, $CFL2^{WT}$ and $CFL2^{V7M}$ were expressed in BL21 (DE3) *E. Coli*, grown to log phase at 37°C in TB medium, and expression was induced with 1 mM isopropyl beta-D-1-thiogalactopyranoside at 18°C for 15 hr. Cells were harvested by centrifugation and stored as pellets at −80°C. Cell pellets were resuspended in 20 mM Tris pH 8.0, 50 mM NaCl, 1 mM DTT, and protease inhibitors, then lysed by sonication. The lysate was cleared at 30,000 *g* for 30 min in a Fiberlite F13–14X50CY rotor (Thermo Fisher Scientific), then loaded on a 5 mL HiTrap HP Q column (GE Healthcare Biosciences). The flow-through, containing $Cof2^{WT}$ or $Cof2^{V7M}$, was dialyzed against 20 mM HEPES pH 6.8, 25 mM NaCl, and 1 mM DTT, loaded on a 5 mL HiTrap SP FF column (GE Healthcare Biosciences), and eluted with a linear gradient of NaCl (20–500 mM). Peak fractions were concentrated and dialyzed against 20 mM Tris pH 8.0, 50 mM KCl, and 1 mM DTT, aliquoted, and stored at −80°C.

Nucleotide exchange assays—To prepare ADP-G-actin, monomeric ATP-bound 2 mM rabbit muscle actin was treated overnight at 4°C with analytical grade anion exchange resin (BioRad), hexokinase (Sigma-Aldrich), and excess ADP. To initiate a reaction, 2 μM ADP-bound actin monomers and the indicated concentration of Cof2 or $Cof2^{V7M}$ in CDT buffer (0.2 mM CaCl2, 0.2 mM DTT, 10 mM Tris pH 8.0), or buffer alone, were mixed and added to 50 μM ε-ATP. A fluorescence spectrophotometer (Photon Technology International) was used to monitor the reaction at 350-nm excitation and 410-nm emission at 25°C for 200 s.

Author Manuscript Author Manuscript Author Manuscript Author Manuscript

TIRF microscopy—To prepare slides, 24 × 60 mm coverslips (Thermo Fisher Scientific) were cleaned by successive sonications as follows: 60 min in detergent, 20 min in 1 M KOH, 20 min in 1 M HCl min, and 60 min in ethanol. Next, coverslips were thoroughly washed with ddH2O, then dried using an N2-stream. Then, each slide was layered with 200 mL of a solution consisting of 80% ethanol pH 2.0, 2 mg/ml methoxy-poly (ethylene glycol)-silane and 2 μg/ml biotin-poly (ethylene glycol)-silane (Laysan Bio Inc.), and incubated for 16 h at 70°C. To assemble flow cells, PEG-coated coverslips were thoroughly rinsed with ddH2O and dried using an N2-stream, then attached to a prepared flow chamber (Ibidi) with double sided tape (2.5 cm × 2 mm × 120 mm) and five min epoxy resin. Immediately prior to use, coverslips were subjected to sequential incubations as follows: 3 min in HEK-BSA (20 mM HEPES pH 7.5, 1 mM EDTA, 50 mM KCl, 1% BSA), 30 s in Streptavidin (0.1 mg/ml in PBS), a fast rinse in HEK-BSA, and then equilibration in 1X TIRF buffer (10 mM imidazole, 50 mM KCl, 1 mM MgCl2, 1 mM EGTA, 0.2 mM ATP, 10 mM DTT, 15 mM glucose, 20 μg/ml catalase, 100 μg/ml glucose oxidase, and 0.5% methylcellulose (4000 cP), pH 7.5).

To measure effects on filament severing, actin monomers (10% OG (Oregon Green)-labeled, 0.5% biotinylated) were first diluted to 1 μM in TIRF buffer, and immediately transferred to a flow chamber. Actin was polymerized at room temperature until filaments reached approximately 10–15 μm in length, then free actin monomers were washed out, and TIRF buffer containing CFL2 or CFL2 ^{V7M} were introduced by flow in. Time-lapse TIRF microscopy was performed using a Nikon-Ti200 inverted microscope equipped with a 150 mW Ar-Laser (Mellot Griot), a TIRF-objective with a N.A. of 1.49 (Nikon Instruments Inc.), and an EMCCD camera (Andor Ixon). Optimal focus was maintained throughout the recordings using the perfect focus system (Nikon Instruments Inc.). Pixel size, 0.27 μm. TIRF data was analyzed using ImageJ software. The background was subtracted prior to analysis using the background subtraction tool (rolling ball radius = 50 pixels).

QUANTIFICATION AND STATISTICAL ANALYSIS

Statistical parameters, levels of significance, and the exact n (number of larvae and muscles) values are indicated in the figure legends. Each experiment was performed in 2 technical replicas. Data were analyzed with Microsoft Excel and GraphPad Prism 8 for Mac. GraphPad Prism was used to analyze data using either Student's unpaired t-test, One-way ANOVA, or Two-way ANOVA. Pearson's correlation coefficient (r) and R^2 values were also computed using GraphPad Prism. Statistical results were presented as means ± SEM and p values of less than 0.05 were considered statistically significant. Asterisks indicate critical levels of significance.

Supplementary Material

Refer to Web version on PubMed Central for supplementary material.

ACKNOWLEDGMENTS

We thank the Baylies lab members for helpful discussions, particularly K. Dobi, for help in making the *Mhc-Gal, Zasp-GFP* stock. We also thank S. Jansen (Washington University) for helpful discussions and technical assistance; K. Anderson, W. Razzell, J. Rosen, and K. Dobi for helpful comments on the manuscript; M. Distinti for help with

Author Manuscript Author Manuscript Author Manuscript Author Manuscript

the figures; and our funding agencies: NIH (R21AR067361, RO1AR108981, and RO1GM121971 to M.K.B.), the National Cancer Institute (P30 CA 008748, core grant to Memorial Sloan Kettering Cancer Center [MSKCC]), and NIH (R01GM063691 to B.L.G.). We thank members of the Electron Microscopy Resource Center at The Rockefeller University, particularly N. Soplop and K. Uryu, for technical assistance.

REFERENCES

Abe H, and Obinata T. (1989). An actin-depolymerizing protein in embryonic chicken skeletal muscle: purification and characterization. J. Biochem 106, 172–180. [PubMed: 2777748]

Abe H, Ohshima S, and Obinata T. (1989). A cofilin-like protein is involved in the regulation of actin assembly in developing skeletal muscle. J. Biochem 106, 696–702. [PubMed: 2691511]

Agrawal PB, Strickland CD, Midgett C, Morales A, Newburger DE, Poulos MA, Tomczak KK, Ryan MM, Iannaccone ST, Crawford TO, et al. (2004). Heterogeneity of nemaline myopathy cases with skeletal muscle alpha-actin gene mutations. Ann. Neurol 56, 86–96. [PubMed: 15236405]

Agrawal PB, Greenleaf RS, Tomczak KK, Lehtokari V-L, Wallgren-Pettersson C, Wallefeld W, Laing NG, Darras BT, Maciver SK, Dormitzer PR, and Beggs AH. (2007). Nemaline myopathy with minicores caused by mutation of the CFL2 gene encoding the skeletal muscle actin-binding protein, cofilin-2. Am. J. Hum. Genet 80, 162–167. [PubMed: 17160903]

Agrawal PB, Joshi M, Savic T, Chen Z, and Beggs AH. (2012). Normal myofibrillar development followed by progressive sarcomeric disruption with actin accumulations in a mouse Cfl2 knockout demonstrates requirement of cofilin-2 for muscle maintenance. Hum. Mol. Genet 21, 2341–2356. [PubMed: 22343409]

Andrianantoandro E, and Pollard TD. (2006). Mechanism of actin filament turnover by severing and nucleation at different concentrations of ADF/cofilin. Mol. Cell 24, 13–23. [PubMed: 17018289]

Bachman JF, Klose A, Liu W, Paris ND, Blanc RS, Schmalz M, Knapp E, and Chakkalakal JV. (2018). Prepubertal skeletal muscle growth requires Pax7-expressing satellite cell-derived myonuclear contribution. Development 145, dev167197.

Bader M, Benjamin S, Wapinski OL, Smith DM, Goldberg AL, and Steller H. (2011). A conserved F box regulatory complex controls proteasome activity in Drosophila. Cell 145, 371–382. [PubMed: 21529711]

Bai J, Hartwig JH, and Perrimon N. (2007). SALS, a WH2-domain-containing protein, promotes sarcomeric actin filament elongation from pointed ends during Drosophila muscle growth. Dev. Cell 13, 828–842. [PubMed: 18061565]

Bamburg JR, and Bray D. (1987). Distribution and cellular localization of actin depolymerizing factor. J. Cell Biol 105, 2817–2825. [PubMed: 3320057]

Bate M. (1990). The embryonic development of larval muscles in Drosophila. Development 110, 791–804. [PubMed: 2100994]

Belote JM, and Fortier E. (2002). Targeted expression of dominant negative proteasome mutants in Drosophila melanogaster. Genesis 34, 80–82. [PubMed: 12324954]

Bennett P, Craig R, Starr R, and Offer G. (1986). The ultrastructural location of C-protein, X-protein and H-protein in rabbit muscle. J. Muscle Res. Cell Motil 7, 550–567. [PubMed: 3543050]

Berger Z, Davies JE, Luo S, Pasco MY, Majoul I, O'Kane CJ, and Rubinsztein DC. (2006). Deleterious and protective properties of an aggregate-prone protein with a polyalanine expansion. Hum. Mol. Genet 15, 453–465. [PubMed: 16371423]

Blair A, Tomlinson A, Pham H, Gunsalus KC, Goldberg ML, and Laski FA. (2006). Twinstar, the Drosophila homolog of cofilin/ADF, is required for planar cell polarity patterning. Development 133, 1789–1797. [PubMed: 16571634]

Brand AH, and Perrimon N. (1993). Targeted gene expression as a means of altering cell fates and generating dominant phenotypes. Development 118, 401–415. [PubMed: 8223268]

Brent JR, Werner KM, and McCabe BD. (2009). Drosophila larval NMJ dissection. J. Vis. Exp (24), 1107. [PubMed: 19229190]

Casella JF, Maack DJ, and Lin S. (1986). Purification and initial characterization of a protein from skeletal muscle that caps the barbed ends of actin filaments. J. Biol. Chem 261, 10915–10921. [PubMed: 3733738]

Author Manuscript Author Manuscript Author Manuscript Author Manuscript

Casella JF, Craig SW, Maack DJ, and Brown AE. (1987). Cap Z(36/32), a barbed end actin-capping protein, is a component of the Z-line of skeletal muscle. J. Cell Biol 105, 371–379. [PubMed: 3301868]

Cassandrini D, Trovato R, Rubegni A, Lenzi S, Fiorillo C, Baldacci J, Minetti C, Astrea G, Bruno C, and Santorelli FM; Italian Network on Congenital Myopathies (2017). Congenital myopathies: clinical phenotypes and new diagnostic tools. Ital. J. Pediatr 43, 101. [PubMed: 29141652]

Chin SM, Jansen S, and Goode BL. (2016). TIRF microscopy analysis of human Cof1, Cof2, and ADF effects on actin filament severing and turnover. J. Mol. Biol 428, 1604–1616. [PubMed: 26996939]

Choi BJ, Imlach WL, Jiao W, Wolfram V, Wu Y, Grbic M, Cela C, Baines RA, Nitabach MN, and McCabe BD. (2014). Miniature neurotrans-mission regulates Drosophila synaptic structural maturation. Neuron 82, 618–634. [PubMed: 24811381]

Demontis F, and Perrimon N. (2009). Integration of Insulin receptor/Foxo signaling and dMyc activity during muscle growth regulates body size in Drosophila. Development 136, 983–993. [PubMed: 19211682]

Dix DJ, and Eisenberg BR. (1990). Myosin mRNA accumulation and myofibrillogenesis at the myotendinous junction of stretched muscle fibers. J. Cell Biol 111, 1885–1894. [PubMed: 2229178]

Edwards KA, Montague RA, Shepard S, Edgar BA, Erikson RL, and Kiehart DP. (1994). Identification of Drosophila cytoskeletal proteins by induction of abnormal cell shape in fission yeast. Proc. Natl. Acad. Sci. USA 91, 4589–4593. [PubMed: 8183953]

Ehler E, and Gautel M. (2008). The sarcomere and sarcomerogenesis. Adv. Exp. Med. Biol 642, 1–14. [PubMed: 19181089]

Farah CS, and Reinach FC. (1995). The troponin complex and regulation of muscle contraction. FASEB J. 9, 755–767. [PubMed: 7601340]

Fernandes I, and Schöck F. (2014). The nebulin repeat protein Lasp regulates I-band architecture and filament spacing in myofibrils. J. Cell Biol 206, 559–572. [PubMed: 25113030]

Fowler VM. (1996). Regulation of actin filament length in erythrocytes and striated muscle. Curr. Opin. Cell Biol 8, 86–96. [PubMed: 8791408]

Graziano BR, Jonasson EM, Pullen JG, Gould CJ, and Goode BL. (2013). Ligand-induced activation of a formin-NPF pair leads to collaborative actin nucleation. J. Cell Biol 201, 595–611. [PubMed: 23671312]

Gunsalus KC, Bonaccorsi S, Williams E, Verni F, Gatti M, and Goldberg ML. (1995). Mutations in twinstar, a Drosophila gene encoding a cofilin/ADF homologue, result in defects in centrosome migration and cytokinesis. J. Cell Biol 131, 1243–1259. [PubMed: 8522587]

Gupta VA, and Beggs AH. (2014). Kelch proteins: emerging roles in skeletal muscle development and diseases. Skelet. Muscle 4, 11. [PubMed: 24959344]

Gurniak CB, Chevessier F, Jokwitz M, Jönsson F, Perlas E, Richter H, Matern G, Boyl PP, Chaponnier C, Fürst D, et al. (2014). Severe protein aggregate myopathy in a knockout mouse model points to an essential role of cofilin2 in sarcomeric actin exchange and muscle maintenance. Eur. J. Cell Biol 93, 252–266. [PubMed: 24598388]

Haas JN. (1950). Cytoplasmic growth in the muscle fibers of larvae of Drosophila melanogaster. Growth 14, 277–294. [PubMed: 14823419]

Halfon MS, Carmena A, Gisselbrecht S, Sackerson CM, Jimé nez F, Baylies MK, and Michelson AM (2000). Ras pathway specificity is determined by the integration of multiple signal-activated and tissue-restricted transcription factors. Cell 103, 63–74. [PubMed: 11051548]

Henderson CA, Gomez CG, Novak SM, Mi-Mi L, and Gregorio CC. (2017). Overview of the Muscle Cytoskeleton. Compr. Physiol 7, 891–944. [PubMed: 28640448]

Ilkovski B, Cooper ST, Nowak K, Ryan MM, Yang N, Schnell C, Durling HJ, Roddick LG, Wilkinson I, Kornberg AJ, et al. (2001). Nemaline myopathy caused by mutations in the muscle alpha-skeletal-actin gene. Am. J. Hum. Genet 68, 1333–1343. [PubMed: 11333380]

Jockusch BM, Veldman H, Griffiths GW, van Oost BA, and Jennekens FG. (1980). Immunofluorescence microscopy of a myopathy. alpha-Actinin is a major constituent of nemaline rods. Exp. Cell Res 127, 409–420. [PubMed: 6991264]

Author Manuscript Author Manuscript Author Manuscript Author Manuscript

Katrukha IA. (2013). Human cardiac troponin complex. Structure and functions. Biochemistry (Mosc.) 78, 1447–1465. [PubMed: 24490734]

Kaya-Çopur A, and Schnorrer F. (2019). RNA Interference Screening for Genes Regulating Drosophila Muscle Morphogenesis. Methods Mol. Biol 1889, 331–348. [PubMed: 30367424]

Kondo E, Nishimura T, Kosho T, Inaba Y, Mitsuhashi S, Ishida T, Baba A, Koike K, Nishino I, Nonaka I, et al. (2012). Recessive RYR1 mutations in a patient with severe congenital nemaline myopathy with ophthalomoplegia identified through massively parallel sequencing. Am. J. Med. Genet. A 158A, 772–778. [PubMed: 22407809]

Kremneva E, Makkonen MH, Skwarek-Maruszewska A, Gateva G, Michelot A, Dominguez R, and Lappalainen P. (2014). Cofilin-2 controls actin filament length in muscle sarcomeres. Dev. Cell 31, 215–226. [PubMed: 25373779]

Labeit S, and Kolmerer B. (1995). The complete primary structure of human nebulin and its correlation to muscle structure. J. Mol. Biol 248, 308–315. [PubMed: 7739042]

Lexell J, Sjöström M, Nordlund AS, and Taylor CC. (1992). Growth and development of human muscle: a quantitative morphological study of whole vastus lateralis from childhood to adult age. Muscle Nerve 15, 404–409. [PubMed: 1557091]

Littlefield RS, and Fowler VM. (2008). Thin filament length regulation in striated muscle sarcomeres: pointed-end dynamics go beyond a nebulin ruler. Semin. Cell Dev. Biol 19, 511–519. [PubMed: 18793739]

Maggi L, Scoto M, Cirak S, Robb SA, Klein A, Lillis S, Cullup T, Feng L, Manzur AY, Sewry CA, et al. (2013). Congenital myopathies–clinical features and frequency of individual subtypes diagnosed over a 5-year period in the United Kingdom. Neuromuscul. Disord 23, 195–205. [PubMed: 23394784]

Malfatti E, and Romero NB. (2016). Nemaline myopathies: state of the art. Rev. Neurol. (Paris) 172, 614–619. [PubMed: 27659899]

Malfatti E, Lehtokari V-L, Böhm J, De Winter JM, Schäffer U, Estournet B, Quijano-Roy S, Monges S, Lubieniecki F, Bellance R, et al. (2014). Muscle histopathology in nebulin-related nemaline myopathy: ultrastrastructural findings correlated to disease severity and genotype. Acta Neuropathol. Commun 2, 44. [PubMed: 24725366]

Mardahl-Dumesnil M, and Fowler VM. (2001). Thin filaments elongate from their pointed ends during myofibril assembly in Drosophila indirect flight muscle. J. Cell Biol 155, 1043–1053. [PubMed: 11739412]

Masaki T, Endo M, and Ebashi S. (1967). Localization of 6S component of a alpha-actinin at Z-band. J. Biochem 62, 630–632. [PubMed: 4870966]

Michelot A, Berro J, Guérin C, Boujemaa-Paterski R, Staiger CJ, Martiel J-L, and Blanchoin L. (2007). Actin-filament stochastic dynamics mediated by ADF/cofilin. Curr. Biol 17, 825–833. [PubMed: 17493813]

Millard TH, and Martin P. (2008). Dynamic analysis of filopodial interactions during the zippering phase of Drosophila dorsal closure. Development 135, 621–626. [PubMed: 18184725]

Miyatake S, Mitsuhashi S, Hayashi YK, Purevjav E, Nishikawa A, Koshimizu E, Suzuki M, Yatabe K, Tanaka Y, Ogata K, et al. (2017). Biallelic Mutations in MYPN, Encoding Myopalladin, Are Associated with Childhood-Onset, Slowly Progressive Nemaline Myopathy. Am. J. Hum. Genet 100, 169–178. [PubMed: 28017374]

Ng J, and Luo L. (2004). Rho GTPases regulate axon growth through convergent and divergent signaling pathways. Neuron 44, 779–793. [PubMed: 15572110]

Nilipour Y, Nafissi S, Tjust AE, Ravenscroft G, Hossein-Nejad Nedai H, Taylor R, Varasteh V, Pedrosa Domellöf F, Zangi M, Tonekaboni SH, et al. (2018). Ryanodine receptor type 3 (RYR3) as a novel gene associated with a myopathy with nemaline bodies. Eur. J. Neurol 25, 841–847. [PubMed: 29498452]

Nworu CU, Kraft R, Schnurr DC, Gregorio CC, and Krieg PA. (2015). Leiomodin 3 and tropomodulin 4 have overlapping functions during skeletal myofibrillogenesis. J. Cell Sci 128, 239–250. [PubMed: 25431137]

Ockeloen CW, Gilhuis HJ, Pfundt R, Kamsteeg EJ, Agrawal PB, Beggs AH, Dara Hama-Amin A, Diekstra A, Knoers NVAM, Lammens M, and van Alfen N. (2012). Congenital myopathy caused

Author Manuscript Author Manuscript Author Manuscript Author Manuscript

by a novel missense mutation in the CFL2 gene. Neuromuscul. Disord 22, 632–639. [PubMed: 22560515]

Ong RW, AlSaman A, Selcen D, Arabshahi A, Yau KS, Ravenscroft G, Duff RM, Atkinson V, Allcock RJ, and Laing NG. (2014). Novel cofilin-2 (CFL2) four base pair deletion causing nemaline myopathy. J. Neurol. Neurosurg. Psychiatry 85, 1058–1060. [PubMed: 24610938]

Ono S. (2010). Dynamic regulation of sarcomeric actin filaments in striated muscle. Cytoskeleton (Hoboken) 67, 677–692. [PubMed: 20737540]

Ono S, Baillie DL, and Benian GM. (1999). UNC-60B, an ADF/cofilin family protein, is required for proper assembly of actin into myofibrils in Caenorhabditis elegans body wall muscle. J. Cell Biol 145, 491–502. [PubMed: 10225951]

Ono K, Parast M, Alberico C, Benian GM, and Ono S. (2003). Specific requirement for two ADF/cofilin isoforms in distinct actin-dependent processes in Caenorhabditis elegans. J. Cell Sci 116, 2073–2085. [PubMed: 12679387]

Pearson AM. (1990). Muscle growth and exercise. Crit. Rev. Food Sci. Nutr 29, 167–196. [PubMed: 2222798]

Ravikumar B, Duden R, and Rubinsztein DC. (2002). Aggregate-prone proteins with polyglutamine and polyalanine expansions are degraded by autophagy. Hum. Mol. Genet 11, 1107–1117. [PubMed: 11978769]

Ravikumar B, Vacher C, Berger Z, Davies JE, Luo S, Oroz LG, Scaravilli F, Easton DF, Duden R, O'Kane CJ, and Rubinsztein DC. (2004). Inhibition of mTOR induces autophagy and reduces toxicity of polyglutamine expansions in fly and mouse models of Huntington disease. Nat. Genet 36, 585–595. [PubMed: 15146184]

Romero NB, Sandaradura SA, and Clarke NF. (2013). Recent advances in nemaline myopathy. Curr. Opin. Neurol 26, 519–526. [PubMed: 23995272]

Ruppel KM, and Spudich JA. (1996). Structure-function analysis of the motor domain of myosin. Annu. Rev. Cell Dev. Biol 12, 543–573. [PubMed: 8970737]

Sandaradura SA, Bournazos A, Mallawaarachchi A, Cummings BB, Waddell LB, Jones KJ, Troedson C, Sudarsanam A, Nash BM, Peters GB, et al. (2018). Nemaline myopathy and distal arthrogryposis associated with an autosomal recessive TNNT3 splice variant. Hum. Mutat 39, 383–388. [PubMed: 29266598]

Sanger JM, and Sanger JW. (2008). The dynamic Z bands of striated muscle cells. Sci. Signal 1, pe37.

Sanoudou D, and Beggs AH. (2001). Clinical and genetic heterogeneity in nemaline myopathy–a disease of skeletal muscle thin filaments. Trends Mol. Med 7, 362–368. [PubMed: 11516997]

Sellers JR. (2000). Myosins: a diverse superfamily. Biochim. Biophys. Acta 1496, 3–22. [PubMed: 10722873]

Sevdali M, Kumar V, Peckham M, and Sparrow J. (2013). Human congenital myopathy actin mutants cause myopathy and alter Z-disc structure in Drosophila flight muscle. Neuromuscul. Disord 23, 243–255. [PubMed: 23294764]

Sewry CA, Laitila JM, and Wallgren-Pettersson C. (2019). Nemaline myopathies: a current view. J. Muscle Res. Cell Motil 40, 111–126. [PubMed: 31228046]

Singh SH, Kumar P, Ramachandra NB, and Nongthomba U. (2014). Roles of the troponin isoforms during indirect flight muscle development in Drosophila. J. Genet 93, 379–388. [PubMed: 25189233]

Stevenson TO, Mercer KB, Cox EA, Szewczyk NJ, Conley CA, Hardin JD, and Benian GM. (2007). unc-94 encodes a tropomodulin in Caenorhabditis elegans. J. Mol. Biol 374, 936–950. [PubMed: 17976644]

Subramanian K, Gianni D, Balla C, Assenza GE, Joshi M, Semigran MJ, Macgillivray TE, Van Eyk JE, Agnetti G, Paolocci N, et al. (2015). Cofilin-2 phosphorylation and sequestration in myocardial aggregates: novel pathogenetic mechanisms for idiopathic dilated cardiomyopathy. J. Am. Coll. Cardiol 65, 1199–1214. [PubMed: 25814227]

Sztal TE, Zhao M, Williams C, Oorschot V, Parslow AC, Giousoh A, Yuen M, Hall TE, Costin A, Ramm G, et al. (2015). Zebrafish models for nemaline myopathy reveal a spectrum of nemaline bodies contributing to reduced muscle function. Acta Neuropathol. 130, 389–406. [PubMed: 25931053]

Author Manuscript Author Manuscript Author Manuscript Author Manuscript

Thirion C, Stucka R, Mendel B, Gruhler A, Jaksch M, Nowak KJ, Binz N, Laing NG, and Lochmüller H. (2001). Characterization of human muscle type cofilin (CFL2) in normal and regenerating muscle. Eur. J. Biochem 268, 3473–3482. [PubMed: 11422377]

Vartiainen MK, Mustonen T, Mattila PK, Ojala PJ, Thesleff I, Partanen J, and Lappalainen P. (2002). The three mouse actin-depolymerizing factor/ cofilins evolved to fulfill cell-type-specific requirements for actin dynamics. Mol. Biol. Cell 13, 183–194. [PubMed: 11809832]

Viswanathan MC, Blice-Baum AC, Schmidt W, Foster DB, and Cammarato A. (2015). Pseudo-acetylation of K326 and K328 of actin disrupts Drosophila melanogaster indirect flight muscle structure and performance. Front. Physiol 6, 116. [PubMed: 25972811]

Wallgren-Pettersson C, Jasani B, Newman GR, Morris GE, Jones S, Singhrao S, Clarke A, Virtanen I, Holmberg C, and Rapola J. (1995). Alpha-actinin in nemaline bodies in congenital nemaline myopathy: immunological confirmation by light and electron microscopy. Neuromuscul. Disord 5, 93–104. [PubMed: 7767098]

Wallgren-Pettersson C, Pelin K, Hilpelä P, Donner K, Porfirio B, Graziano C, Swoboda KJ, Fardeau M, Urtizberea JA, Muntoni F, et al. (1999). Clinical and genetic heterogeneity in autosomal recessive nemaline myopathy. Neuromuscul. Disord 9, 564–572. [PubMed: 10619714]

Wallgren-Pettersson C, Pelin K, Nowak KJ, Muntoni F, Romero NB, Goebel HH, North KN, Beggs AH, and Laing NG; ENMC International Consortium On Nemaline Myopathy (2004). Genotype-phenotype correlations in nemaline myopathy caused by mutations in the genes for nebulin and skeletal muscle alpha-actin. Neuromuscul. Disord 14, 461–470. [PubMed: 15336686]

Windner SE, Manhart A, Brown A, Mogilner A, and Baylies MK. (2019). Nuclear Scaling Is Coordinated among Individual Nuclei in Multinucleated Muscle Fibers. Dev Cell 49, 48–62. [PubMed: 30905770]

Yamaguchi M, Robson RM, Stromer MH, Dahl DS, and Oda T. (1982). Nemaline myopathy rod bodies. Structure and composition. J. Neurol. Sci 56, 35–56. [PubMed: 6754876]

Yang H, Schmidt LP, Wang Z, Yang X, Shao Y, Borg TK, Markwald R, Runyan R, and Gao BZ. (2016). Dynamic Myofibrillar Remodeling in Live Cardiomyocytes under Static Stretch. Sci. Rep 6, 20674. [PubMed: 26861590]

Young P, Ehler E, and Gautel M. (2001). Obscurin, a giant sarcomeric Rho guanine nucleotide exchange factor protein involved in sarcomere assembly. J. Cell Biol 154, 123–136. [PubMed: 11448995]

Zhang S, and Bernstein SI. (2001). Spatially and temporally regulated expression of myosin heavy chain alternative exons during Drosophila embryogenesis. Mech. Dev 101, 35–45. [PubMed: 11231057]

Author Manuscript Author Manuscript Author Manuscript Author Manuscript

Highlights

- *Dm*CFL knockdown results in larval sarcomere deterioration and muscle weakness
- *Dm*CFL loss impairs sarcomere addition and mimics aspects of nemaline myopathy (NM)
- Proteasome activation delays progression of muscle defects in *Dm*CFL knockdown
- NM patient CFL2 mutation alters actin severing and nucleotide exchange rate

Author Manuscript
Author Manuscript
Author Manuscript
Author Manuscript

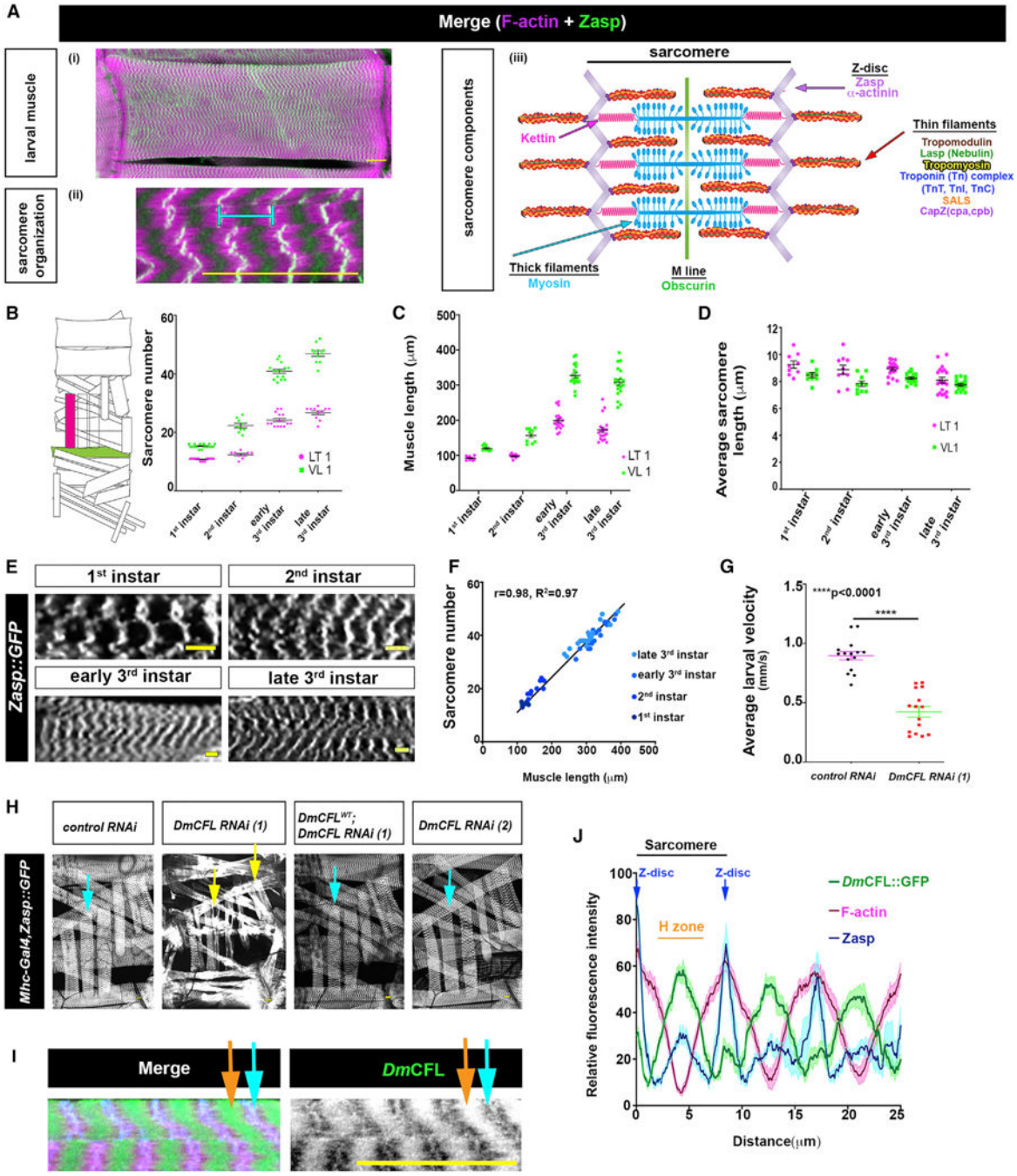

Figure 1. Muscle-Specific Knockdown of *Dm*CFL Affects Muscle Structure and Function during Muscle Growth

(A) Sarcomere organization in a 3rd-instar *Drosophila* larval muscle (Z disc [α-Zasp, green] and F-actin [phalloidin, magenta]) (i and ii). The blue line indicates one sarcomere in (ii). (iii) Schematic depicting a single sarcomere with its structural components: Z discs, thin filaments, and thick filaments. *Drosophila* proteins analyzed in this study and their location within the sarcomere are marked in corresponding colors.

(B–D) Quantification of sarcomere number (B), muscle length (C), and average sarcomere length (D) in LT1 (magenta) and VL1 (green) muscles at each larval instar. One muscle

Author Manuscript Author Manuscript Author Manuscript Author Manuscript

hemisegment, indicating the position of both muscles is shown in (B). n = 15 muscles from ≥5 *control RNAi* larva/instar.

(E) Z disc pattern (Zasp-GFP) at the different larval instar stages.

(F) Linear scaling relationship (line) between VL muscle cell length and sarcomere number across larval stages. Pearson's correlation coefficient (r) and R^2 are indicated.

(G) Crawling velocities of early 3rd-instar larvae expressing *Mhc-Gal4* and the indicated *RNAi*. n = 15 larvae/genotype. p value by unpaired t test.

(H) Single hemisegment of 3rd-instar larval muscles showing Zasp-GFP expression. Blue arrows: wild-type sarcomere/Z disc pattern; yellow arrows: disorganized sarcomeres and Zasp aggregates.

(I) *Dm*CFL-GFP localization (α-GFP, green [left], grayscale [right]), F-actin (phalloidin, magenta), and Zasp protein (α-Zasp, blue) in larval sarcomeres. Orange arrow: H zone; blue arrow: Z disc.

(J) Relative average fluorescence intensities of proteins in (I) across the length of 4 sarcomeres. n = 10 measurements, from ≥5 different muscles from 5 larvae. Endogenous *Dm*CFL-GFP pattern in Figure S1J.

Error bars: mean ± SEM (D, G, and J). Scale bars: 25 mm (A, H, and I) and 8 mm (E). See also Figure S1.

Author Manuscript Author Manuscript Author Manuscript Author Manuscript

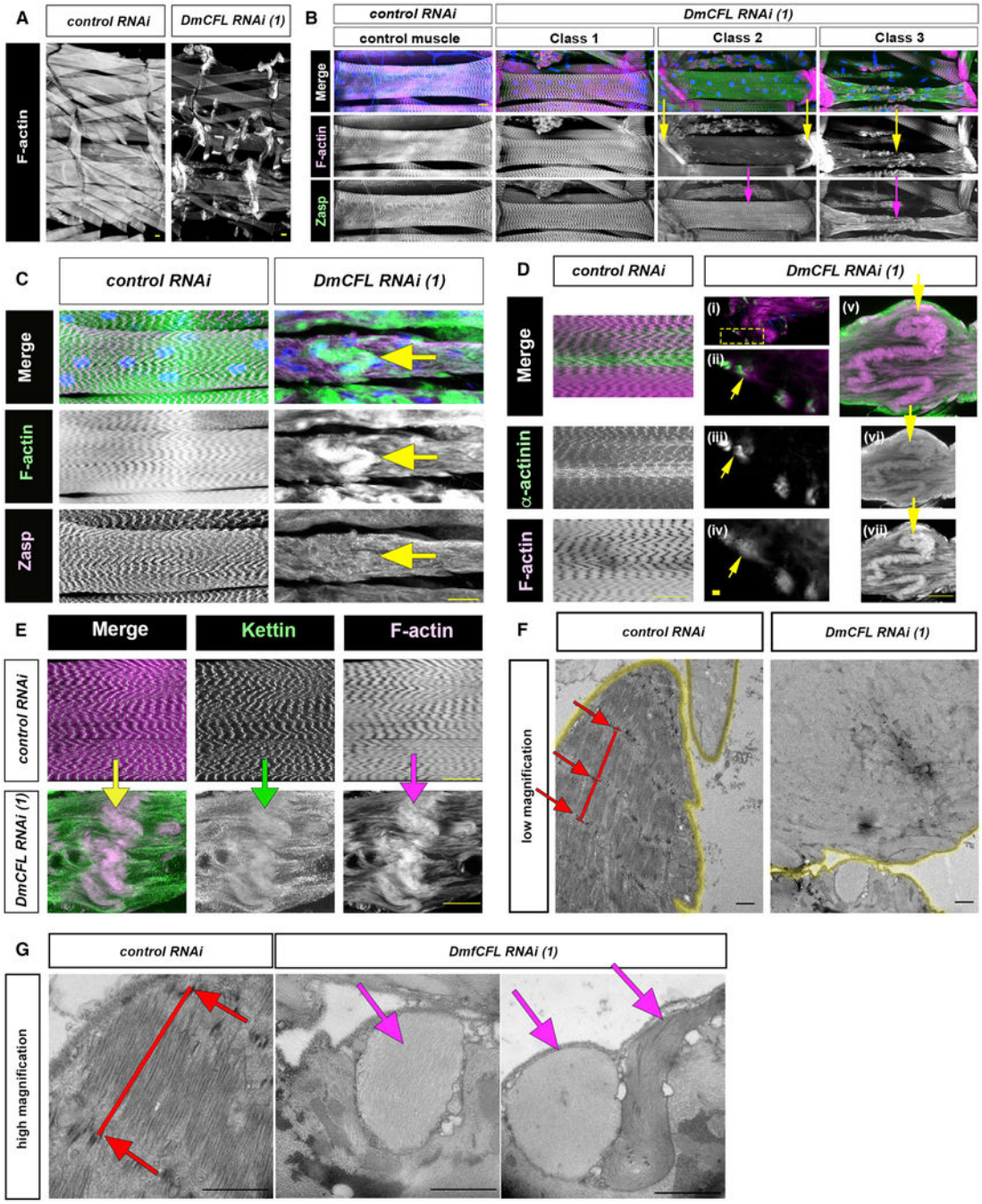

Figure 2. *Dm*CFL Knockdown Results in 3 Classes of Muscle Phenotypes.

Larval muscles at the 3rd-instar stage expressing either *control RNAi* or *DmCFL RNAi (1)* driven with *Mhc-Gal4*..

(A) Lateral view of a single larval hemisegment. Muscles are stained with phalloidin (F-actin)..

(B) Classification of muscle phenotypes using VL3 muscles, labeled with phalloidin (F-actin, magenta), α-Zasp (Zasp, green), and Hoechst (nuclei, blue). n = 200 muscles from 8 larvae/genotype..

Author Manuscript Author Manuscript Author Manuscript Author Manuscript

(C–G) Organization of sarcomeric proteins in control and class 3 muscle cells with severe sarcomere disorganization and protein aggregates (arrows)..

(C–E) Protein aggregates in class 3 VL3 muscles contain F-actin (phalloidin) and the Z disc proteins Zasp (C, magenta), α-actinin (D, green) and kettin (E, green). The arrows indicate protein aggregates. The yellow box in (D, i) denotes the region magnified in subsequent panels showing single z slices (ii–iv)..

(F and G) TEMs of larval muscles at low (F) and high (G) magnification. The control muscles show organized sarcomeres (indicated by red line, with 2 highlighted in F, 1 in G) and Z discs (red arrows). *Dm*CFL-knockdown muscles have aberrant protein aggregates in the cell periphery (indicated in magenta). The yellow lines (G) outline the individual muscles..

Scale bars: 25 μm (A–E), 1 μm (F), and 1 μm (G).

Author Manuscript Author Manuscript Author Manuscript Author Manuscript

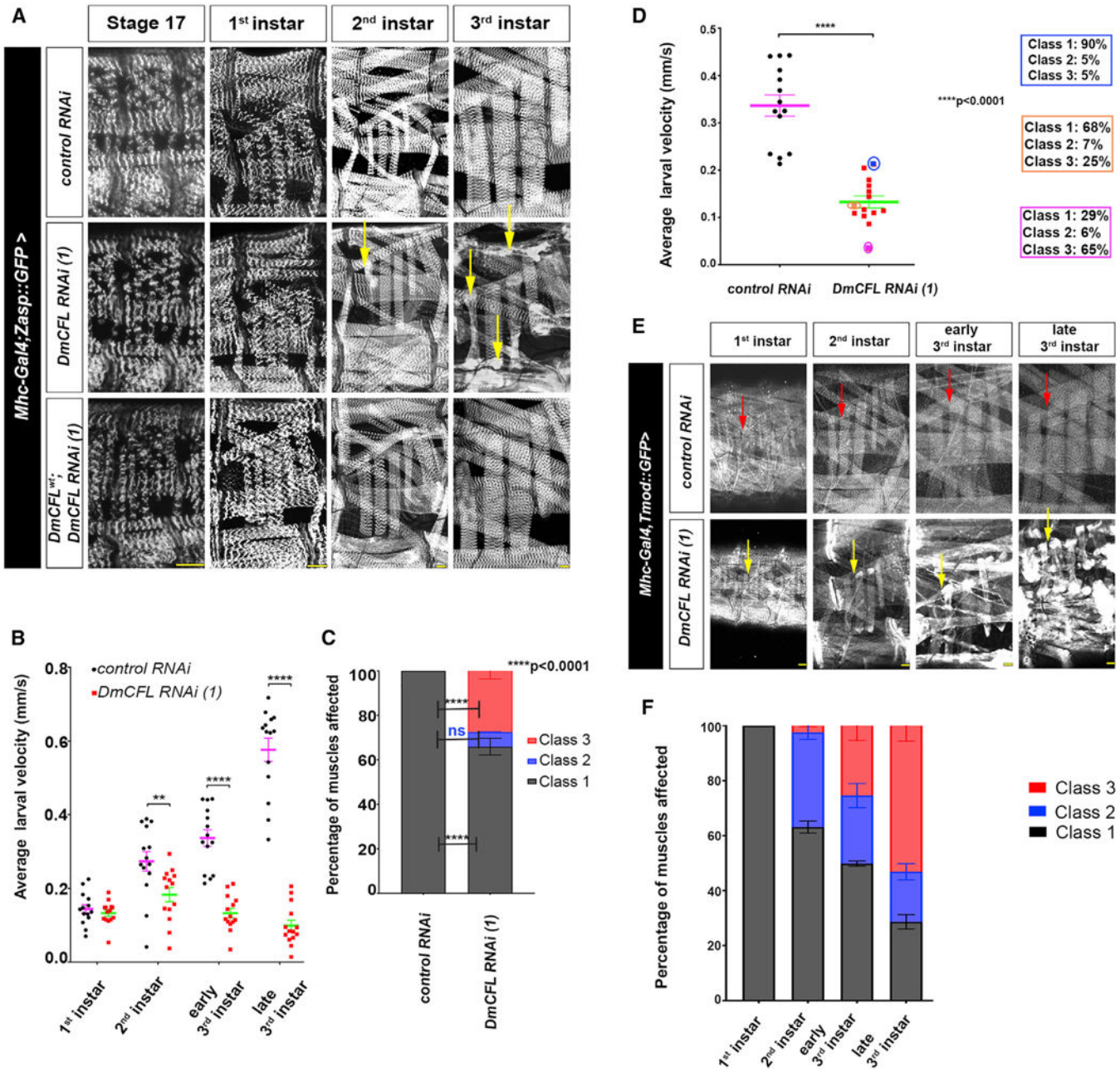

Figure 3. *Dm*CFL Knockdown Results in Progressive Loss of Muscle Structure and Function.

(A) Sarcomere pattern (Zasp-GFP) in larval muscles, from late embryogenesis (stage 17) through the different larval instars. Yellow arrows, sarcomeric structure defects..

(B) Crawling velocities of larvae at different larval stages. p values by multiple t tests. **p < 0.02 and ****p < 0.0001. n = 15 larvae/genotype..

(C) Percentage of different muscle classes at early 3rd-instar stage. *Control RNAi* (100.0% ± 0% wild-type pattern) and *DmCFL RNAi (1)* (class 1: 65.87% ± 3.76%, class 2: 6.63% ± 0.07%, class 3: 27.49% ± 3.69%). p values by 2-way ANOVA (****p < 0.0001). n = 800 muscles/genotype, from ≥8 larvae..

Author Manuscript Author Manuscript Author Manuscript Author Manuscript

(D) Crawling velocities in 3rd-instar larvae. The percentage of muscle classes is shown for 3 individual larvae. p values by unpaired t test. ****p < 0.0001, n = 15 larvae, n = 125 muscles/larva..

(E) Two individual larvae imaged over 4 consecutive days. Muscle cells/sarcomeres are visualized with Tmod-GFP (grayscale). The red arrows in control and the yellow arrows in *DmCFL RNAi (1)* show theprogression of a single muscle over time..

(F) Percentage of muscle classes in *Dm*CFL-knockdown larvae at each stage of larval development. 1st instar (class 1: 100% ± 0.0%), 2nd-instar (class 1: 63.11% ± 2.18%, class 2: 34.47% ± 2.5%, class 3: 2.42% ± 0.32%), early 3rd-instar (class 1:49.81% ± 0.94, class 2: 24.76% ± 4.40%, class 3: 25.42% ± 5.34%), and late 3rd-instar (class 1: 28.67% ± 2.63%, class 2: 18.20% ± 2.93, class 3: 53.121% ± 5.56%). n = 200 muscles/genotype, from ≥5 larvae/stage. Statistical comparison in Figure S2C..

Error bars: mean ± SEM (B, C, D, and F). Scale bars: 25 μm (A and D). See also Figure S2.

Author Manuscript Author Manuscript Author Manuscript Author Manuscript

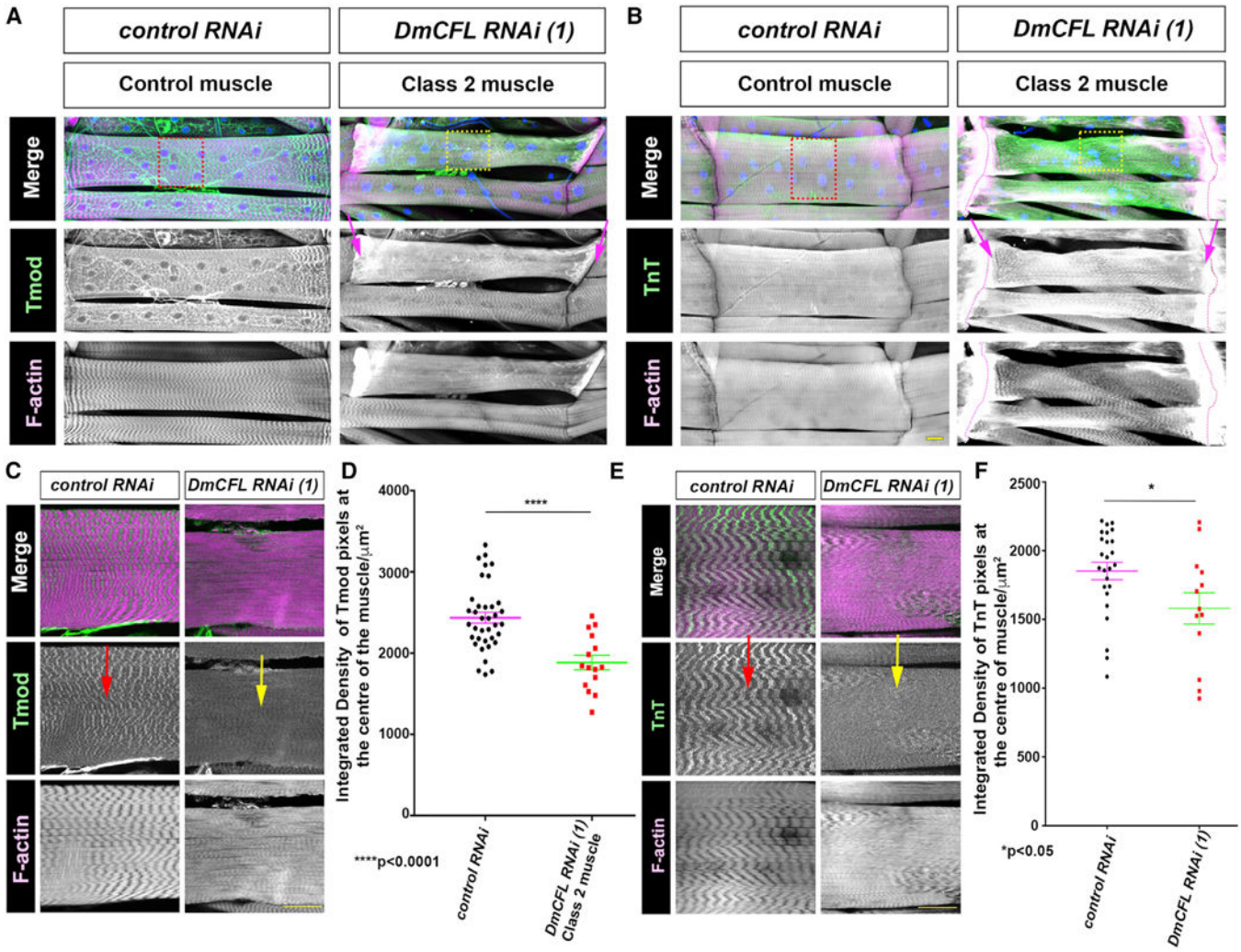

Figure 4. Actin Aggregates in *Dm*CFL-Knockdown Muscles Recruit Sarcomeric Tropomodulin and Troponin.

Analysis of Tmod, TnT (green), and F-actin (phalloidin, magenta) protein localization in VL3 muscles in 3rd-instar larvae expressing *Mhc-Gal4* to drive *control* or *DmCFL RNAi (1)*. In controls, Tmod (A, C, and D) localizes to the M-line and TnT (B, E, and F) localizes to the pointed ends of actin filaments. In class 2 muscles, Tmod and TnT localize to sarcomeres and are enriched at muscle cell poles (magenta arrows), similar to actin. The dotted red and yellow boxes in (A) and (B) are the regions magnified in (C) and (E) and quantified in (D) and (F). The dotted pink lines (B) demarcate the muscle ends. (D and F) Quantification of Tmod and TnT levels at the center of the muscle cells in pixel intensity per square micron. p values by unpaired t test (****$p < 0.0001$). $N \geq 10$ muscles from ≥5 different larvae. Error bars: mean ± SEM (D and F). Scale bars: 25 μm (A–C and E). See also Figures S3 and S4.

Author Manuscript Author Manuscript Author Manuscript Author Manuscript

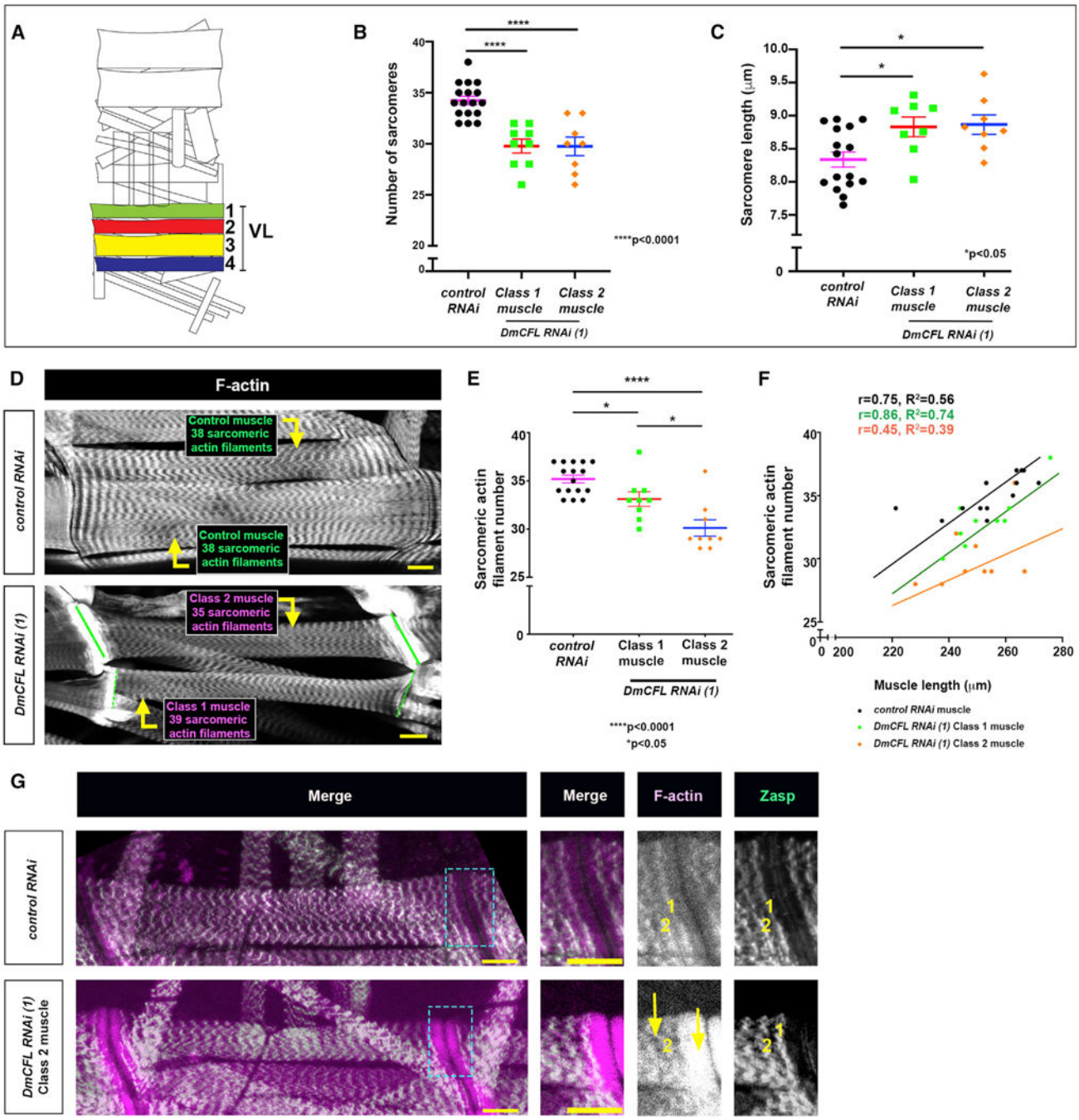

Figure 5. *Dm*CFL Knockdown Affects Sarcomeric Actin Filament Addition at Growing Muscle Ends.

(A) Diagram of 1 hemisegment of the larval musculature, with VL muscles 1–4 highlighted in different colors..

(B and C) Quantification of the number of Z discs (B) and sarcomere length (C), using Zasp-GFP, in VL muscles shown in (A) of the indicated genotypes. p values calculated by unpaired t test. Error bars: mean ± SEM. N ≥ 12 muscles from ≥5 larvae..

(D) VL muscles stained with phalloidin for F-actin (grayscale). In controls, adjacent VL muscles have the same length and number of sarcomeric F-actin bands (38 each). In

Author Manuscript Author Manuscript Author Manuscript Author Manuscript

*Dm*CFL-knockdown muscles of the same length, a class 1 muscle contains 39 F-actin bands, while a class 2 muscle contains only 35 F-actin bands. The dotted lines demarcate the muscle ends..

(E) Quantification of sarcomeric F-actin bands in VL muscles, as indicated in (D). N ≥ 12 muscles from ≥5 larvae..

(F) Plot of muscle cell length (mm) versus the number of sarcomeric F-actin bands in VL muscles. Pearson's correlation coefficient (r) and R^2 values and best-fit lines were calculated for each muscle cell class..

(G) VL muscles stained for F-actin (magenta) and Zasp (green). (Left) Low-magnification merged image of entire VL muscle. Dotted box, region magnified at right. (Right) High-magnification image of sarcomeres at the muscle poles. 1 and 2 denote sarcomeres from muscle pole inward..

Error bars: mean ± SEM (B, C, and E). Scale bar, 25 μm (D and G). See also Figure S5.

Author Manuscript
Author Manuscript
Author Manuscript
Author Manuscript

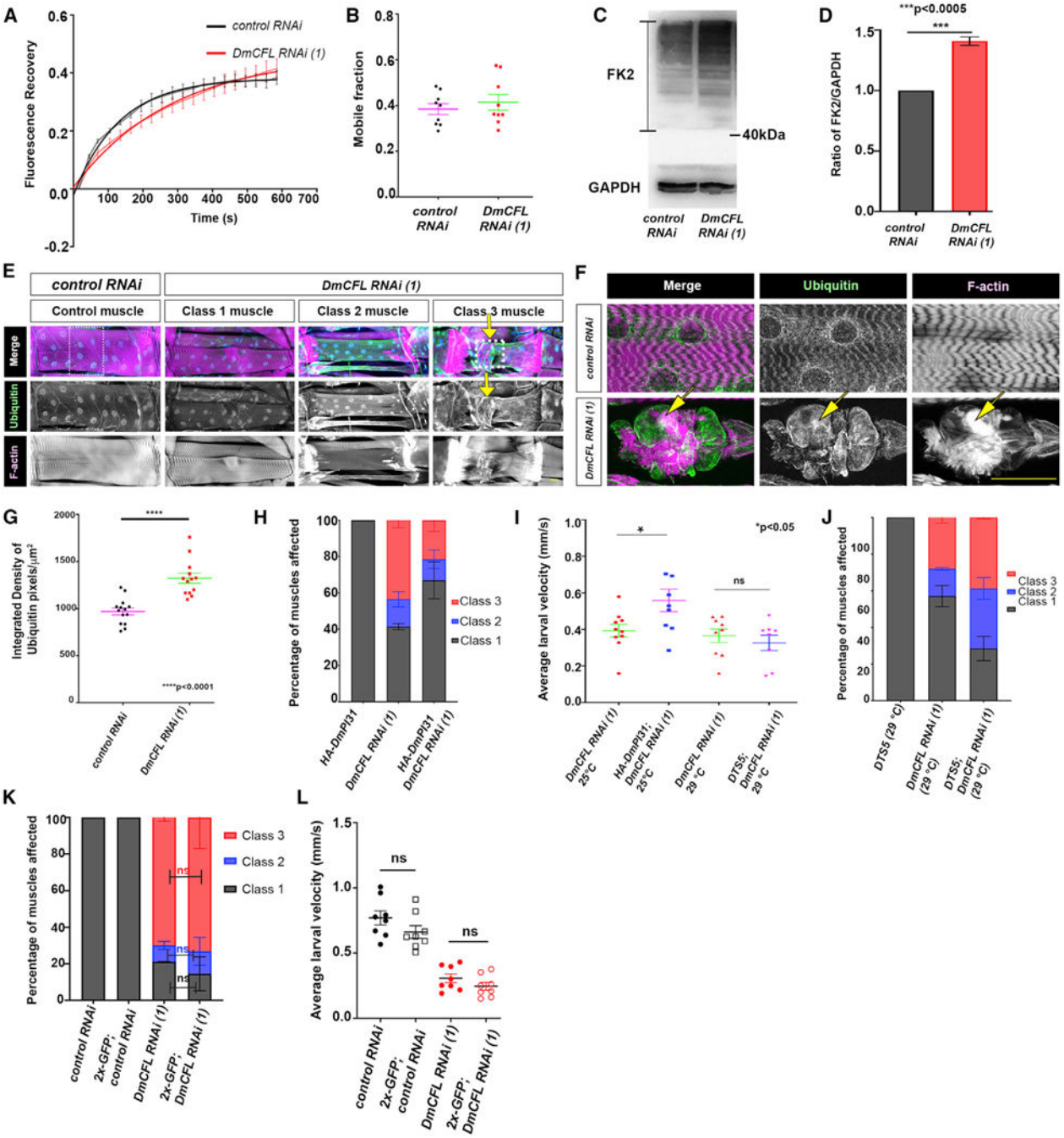

Figure 6. Modulating Proteasome Activity Affects the Progression of Structural and Functional Changes in *Dm*CFL-Knockdown Muscles.

(A) Quantification of Zasp-GFP FRAP in control and class 3 muscle cells in 3rd-instar larvae. n = 9 muscles/genotype..

(B) Mobile fraction analysis of Zasp-GFP in (A). p values by unpaired t test (p = 0.685, ns)..

(C) Western blot of mono- and poly-ubiquitinated protein abundance in 3rd-instar larval carcasses. Glyceraldehyde 3-phosphate dehydrogenase (GAPDH), loading control. Quantification in (D)..

Author Manuscript Author Manuscript Author Manuscript Author Manuscript

(D) Quantitative measurement of (C). Ub levels normalized to GAPDH. n = 20 carcasses. p values by unpaired t test (***p < 0.0005)..

(E) VL3 muscles from 3rd-instar larvae labeled for mono-and poly-ubiquitin (α-FK2, green), F-actin (phalloidin, magenta), and nuclei (Hoechst, blue). n = 8 larvae/ genotype. FK2 levels quantified in (G). Dotted boxes magnified in (F)..

(F) High magnification of muscles as shown in (E). In class 3 muscles, FK2 co-localizes with sarcomeric protein aggregates (yellow arrows)..

(G) Quantification of α-FK2 labeling (pixel intensity values/μm^2) in whole VL muscles, as in (E). p values by unpaired t test (****p < 0.0001). N ≥ 13 muscles from ≥5 larvae..

(H) Percentage of different muscle classes from 3rd-instar larvae expressing *DmCFL RNAi (1)* (class 1:41.403% ± 1.68%, class 2:15.09% ± 4.17%, class 3:43.5% ± 4.11%) or *HA::DmPI31*;*Dm*CFL *RNAi (1)* (class 1:66.87% ± 10.05%, class 2: 11.59% ± 5.08%, class 3: 21.52% ± 6.12%). n = 800 muscles/genotype from ≥8 larvae. Statistical analysis in Figure S6F..

(I) Crawling velocities of 3rd-instar larvae. p values by unpaired t test (*p < 0.05, ns p = 0.498). n = 9 larvae/genotype..

(J) Percentage of different muscle classes in 3rd-instar larvae expressing *DmCFL RNAi (1)* (class 1: 57.14% ± 5.7%, class 2: 14.8% ± 0.68%, class 3: 28.99% ± 4.09%) or *DTS5*;*DmCFL RNAi (1)* (class 1: 28.53% ± 6.62%, class 2: 32.72% ± 5.9%, class 3: 38.74% ± 0.72%). n = 800 muscles/genotype, from ≥8 larvae. Statistical analysis in Figure S6F..

(K) Percentage of different muscle classes in 3rd-instar larvae expressing *DmCFL RNAi (1)* (class 1: 21.085% ± 0.167%, class 2: 9.012% ± 2.181%, class 3:69.903% ± 4.11%), or *2x-GFP*; *DmCFL RNAi (1)* (class 1: 14.540% ± 9.296%, class 2: 12.314% ± 7.612%, class 3:73.146% ± 16.908%). Statistical analysis by 2-way ANOVA. n = 800 muscles/genotype, from ≥8 larvae..

(L) Crawling velocities of 3rd-instar larvae. p values by unpaired t test. n = 9 larvae/ genotype..

Error bars: mean ± SEM (A, B, D, and G–L). Scale bars: 25 μm (E and F). See also Figure S6.

Author Manuscript Author Manuscript Author Manuscript Author Manuscript

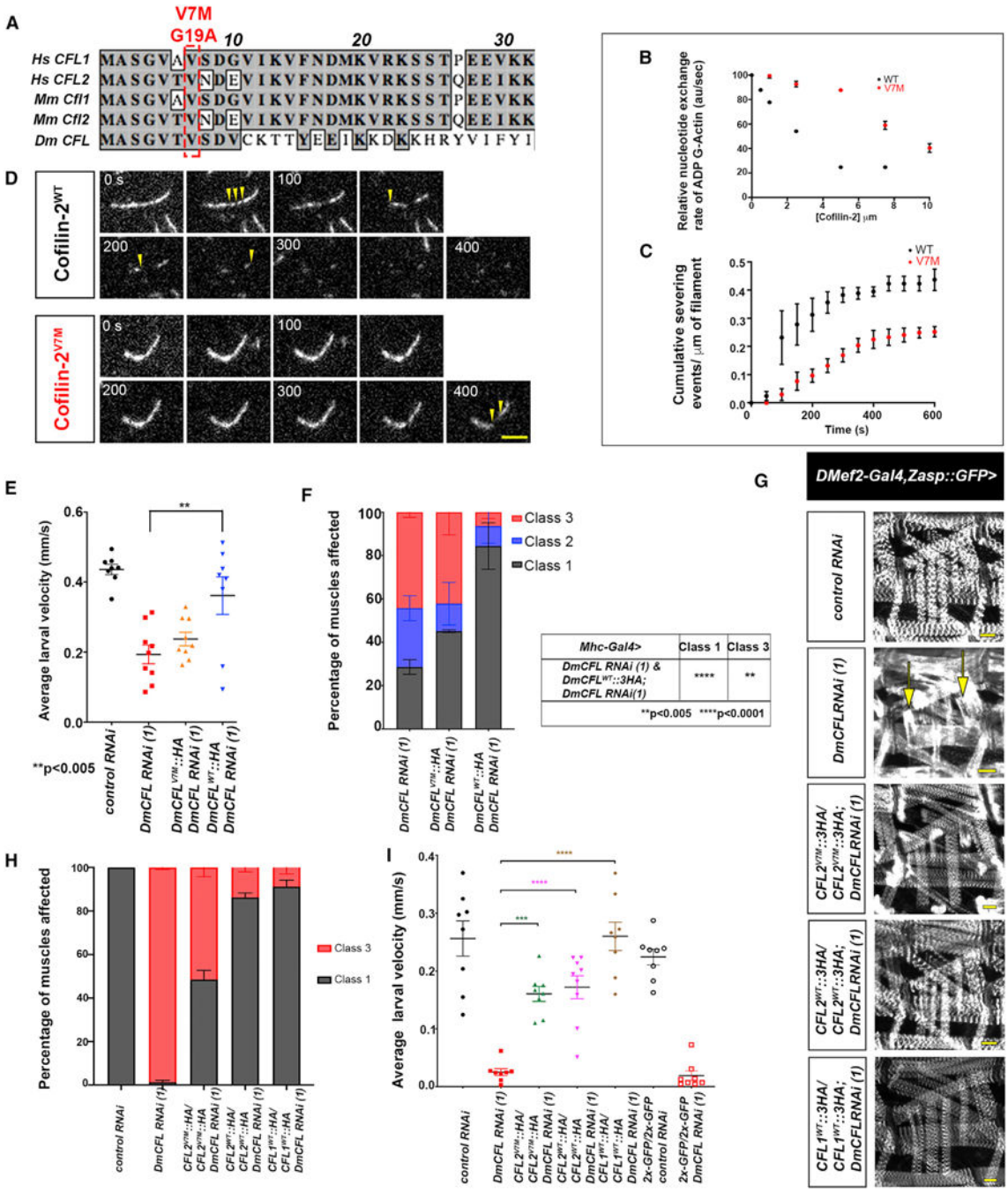

Figure 7. *In Vivo* and *In Vitro* Analyses Identify Phenotypic and Biochemical Consequences of a Specific Patient *CFL2* Mutation.

(A) Sequence alignment of the first 30 amino acids of the proteins encoded by specified genes. There is strong conservation between sequences (gray; entire protein sequences in Figure S7A). Val7 conserved in all 5 proteins. Val7Met (V7M) mutation in *HsCFL2* seen in NM patients..

(B) Comparison of nucleotide exchange rate on 2 μM ADP-actin monomers in the presence of different concentrations of human $CFL2^{WT}$ and $CFL2^{V7M}$..

Author Manuscript Author Manuscript Author Manuscript Author Manuscript

(C) Analysis of actin filament-severing activity. Each data point is the number of cumulative severing events per micron of F-actin at that time point, averaged from 3 independent experiments (n = 20 actin filaments each)..

(D) Representative time-lapse images from TIRF microscopy experiments in which tethered OG (Oregon Green)-labeled actin filaments were preassembled, and then 150 nM $CFL2^{WT}$ or $CFL2^{V7M}$ was flowed in. The severing events (yellow arrowheads) are quantified in Figure S7B. Bar, 5 μm..

(E) Crawling velocities of late 3rd-instar larvae with the indicated genotypes. p values by ordinary 1-way ANOVA (**p < 0.005)..

(F) Percentage of different muscle cell classes in 3rd-instar larvae of the specified genotypes. *DmCFL RNAi (1)* (class 1: 28.57% ± 3.38%, class 2: 27.10% ± 5.75%, class 3: 44.31% ± 2.37%), $DmCFL^{WT}$; *DmCFL RNAi* (class 1: 84.44% ± 10.73%, class 2: 9.13% ± 7.90%, class 3: 6.42% ± 2.83%), and $DmCFL^{V7M}$; *DmCFL RNAi (1)* (class 1: 45.11% ± 0.57%, class 2: 12.66% ± 9.83%, class 3:42.21% ± 10.41%). n = 800 muscles/genotype, from ≥8 larvae. p values by 2-way ANOVA (**p < 0.005 and ****p < 0.0001)..

(G) Sarcomere pattern (grayscale, Zasp-GFP) in muscles from 2nd-instar larvae of specified genotypes. Sarcomeric structure defects (yellow arrows). Bar: 25 μm..

(H) Percentage of different muscle cell classes in 3rd-instar larvae of the specified genotypes. *DmCFL RNAi (1)* (class 1: 1.294% ± 0.887%, class 3: 98.706% ± 0.887%), $HsCFL2^{WT}$; *DmCFL RNAi (1)* (class 1: 86.249% ± 2.025, class 3: 13.751% ± 2.025%), $HsCFL1^{WT}$; *DmCFL RNAi (1)* (class 1: 91.251% ± 2.930, class 3: 8.749% ± 2.930%), and $HsCFL2^{V7M}$; *DmCFL RNAi (1)* (class 1: 48.503% ± 4.185%, class 3: 51.497% ± 4.185%). n = 600 muscles/genotype, from ≥8 larvae. Statistical analysis in Figure S8I..

(I) Crawling velocities of 2nd-instar larvae in which *Dmef2-Gal4* drives the expression of constructs. Velocities of *control RNAi* and *2x-GFP/2x-GFP;control RNAi* larvae (n.s., p = 0.355) and *DmCFL RNAi (1)* and *2x-GFP/2x-GFP;DmCFL RNAi (1)* larvae (n.s., p = 0.569). n = 8 larvae/genotype. p values by ordinary 1-way ANOVA (***p < 0.0002 and ****p < 0.0001). Statistical analysis in Figure S8I..

Error bars: mean ± SEM (B, C, E, F, H, and I). See also Figures S7 and S8.

Author Manuscript Author Manuscript Author Manuscript Author Manuscript

KEY RESOURCES TABLE

REAGENT or RESOURCE	SOURCE	IDENTIFIER
Antibodies		
Mouse anti-Myosin heavy chain	From S.Abmayr (Stowers)	N/A
Chicken anti-GFP	Abcam	Cat#13970; RRID:AB_300798
Rabbit anti-Zasp	From F.Schöck (McGill)	N/A
Rabbit anti-Lasp	From F.Schöck (McGill)	N/A
Rat anti-Tropomodulin	From V.Fowler (Scripps)	N/A
Rat anti-alpha-actinin	Abcam	Cat#ab50599; RRID:AB_867496
Rabbit anti-Obscurin	From B.Bullard (York)	N/A
Rabbit anti-Cpa	From F.Janody (Porto)	N/A
Rat anti-HA	Roche	Cat#11867423001;RRID: AB_390918
Rabbit anti-SALS	From N. Perrimon (Harvard)	N/A
Rat anti-Kettin	Abcam	Cat#ab50585; RRID:AB_873910
Rat anti-Troponin-T	Babraham Institute	Cat#BT-GB1455
Mouse anti-FK2	Enzo Life Sciences	Cat# BML-PW8810; RRID:AB_10541840
Mouse anti-GFP	Roche	Cat#11814460001; RRID:AB_390913
Mouse anti-GAPDH	Abcam	Cat#ab9484; RRID: AB_307274
Alexa Fluor 488-, 555-, and 647-conjugated fluorescent secondary antibodies	Life Technologies	N/A
Peroxidase-conjugated Donkey anti-Rat	Jackson Immunoresearch	Cat#712–035-150
Peroxidase-conjugated Donkey anti-Mouse	Jackson Immunoresearch	Cat#715–035-151
Experimental Models: Organisms/Strains		
D. melanogaster: *DMef2-Gal4*	(Halfon et al., 2000)	N/A
D. melanogaster: *Mhc-Gal4*	Bloomington Drosophila Stock Center	BDSC# 67044
D. melanogaster: *UAS-mCherry-RNAi*	Bloomington Drosophila Stock Center	BDSC# 35785
D. melanogaster: *UAS-tsr-RNAi (HMS00534)*	Bloomington Drosophila Stock Center	BDSC #65055
D. melanogaster: *UAS-2x-GFP*	Bloomington Drosophila Stock Center	BDSC # 6874
D. melanogaster: *Tmod::GFP*	Bloomington Drosophila Stock Center	BDSC #50861
D. melanogaster: *Zasp66::GFP (ZCL0663)*	Bloomington Drosophila Stock Center	BDSC #6824
D. melanogaster: tsr^{N96A}	Bloomington Drosophila Stock Center	BDSC# 9108
D. melanogaster: *UAS-tsr-IR*	Vienna Drosophila Resource Centre	VDRC #110599
D. melanogaster: *tsr::GFP (ZCL2393)*	Kyoto Stock Center	DGRC #110875

Author Manuscript Author Manuscript Author Manuscript Author Manuscript

REAGENT or RESOURCE	SOURCE	IDENTIFIER
D. melanogaster: *UAS-HA-PI31*	(Bader et al., 2011)	N/A
D. melanogaster: *UAS-DTS5*	(Bader et al., 2011)	N/A
D. melanogaster: *UAS-moesin::mCherry*	(Millard and Martin, 2008)	N/A
D. melanogaster: UAS-tsr^{V7M}::3HA	This study	N/A
D. melanogaster: UAS-tsr^{WT}::3HA	This study	N/A
D. melanogaster: UAS-human Cof2^{V7M}::3HA	This study	N/A
D. melanogaster: UAS-human Cof2^{WT}::3HA	This study	N/A
D. melanogaster: UAS-human Cof2^{WT}::3HA	This study	N/A
Oligonucleotides		
Primer: Forward Primer to clone *DmCFL^{WT}* (5′-CAC CGAATTCATGGCTTCTGGTGTAACTGTGTCT-3′)	This study	N/A
Primer: Reverse Primer to clone *DmCFL^{WT}* (5′-CAC CGAATTCATGGCTTCTGGTGTAACTATGTCTGAT GTCTGCAAGACTACAT-3′)	This study	N/A
Primer: Forward Primer to clone *DmCFL^{V7M}* (5′-CAC CGAATTCATGGCTTCTGGTGTAACTATG TCTGATG TCTGCAAGACTACAT-3′)	This study	N/A
Primer: Reverse Primer to clone *DmCFL^{V7M}* (5′-CAC CGAATTCATGGCTTCTGGTGTAACTATGTCTGATG TCTGCAAGACTACAT-3′)	This study	N/A
Primer: Forward Primer to clone human *CFL2^{WT}* (5′ - CACCGAATTCATGGCTTCTGGAGTTACA GTG AAT-3′)	This study	N/A
Primer: Reverse Primer to clone human *CFL2^{WT}* (5′-GGATCCTAATGGTTTTCCTTCAAGTGAAA CT-3′)	This study	N/A
Primer: Forward Primer to clone human *CFL2^{V7M}* (5′-CACCGAATTCATGGCTTCTGGAGTTACAA TGAA TGATGAAGTCATCAAAGTTTTT-3′)	This study	N/A
Primer: Reverse Primer to clone human *CFL2^{V7M}* (5′GGATCCTAATGGTTTTCCTTCAAGTGAAACT-3′)	This study	N/A
Primer: Forward Primer to clone human *CFL1^{WT}* (5′- CACCGAATTCATGGCCTCCGGTGTGGCT GTCT-3′)	This study	N/A
Primer: Reverse Primer to clone human *CFL1^{WT}* (5′- GGATCCCAAAGGCTTGCCCTCCAGGGA G-3′)	This study	N/A
Recombinant DNA		
Plasmid: pENTR	Life Technologies	Cat#K240020
Plasmid: pTWH	DGRC	Cat# 1100
Plasmid: pUASg-3xHA.attB	From Konrad Basler (Zurich)	N/A
Software and Algorithms		
ImageJ/Fiji	NH	https://fiji.sc; RRID: SCR_002285
GraphPad Prism	GraphPad	https://www.graphpad.com; RRID:SCR_002798
Photoshop	Adobe	https://www.adobe.com/products/photoshop.html; RRID:SCR_014199

Author Manuscript

Author Manuscript

Author Manuscript

Author Manuscript

REAGENT or RESOURCE	SOURCE	IDENTIFIER
Illustrator	Adobe	https://www.adobe.com/products/illustrator.html; RRID:SCR_010279
Excel	Microsoft	https://www.microsoft.com/en-gb/; RRID: SCR_016137
MacVector	MacVector Inc.	https://macvector.com; RRID:SCR_015700
Imaris	BitPlane	https://imaris.oxinst.com/packages; RRID: SCR_007370